



HAL
open science

Loss of Energetic Ions Comprising the Ring Current Populations of Jupiter's Middle and Inner Magnetosphere

B. H. Mauk, F. Allegrini, F. Bagenal, S. J. Bolton, G. Clark, J. E. P. Connerney, D. J. Gershman, D. K. Haggerty, V. Hue, M. Imai, et al.

► **To cite this version:**

B. H. Mauk, F. Allegrini, F. Bagenal, S. J. Bolton, G. Clark, et al.. Loss of Energetic Ions Comprising the Ring Current Populations of Jupiter's Middle and Inner Magnetosphere. *Journal of Geophysical Research Space Physics*, 2022, 127, 10.1029/2022JA030293 . insu-03867494

HAL Id: insu-03867494

<https://insu.hal.science/insu-03867494>

Submitted on 23 Nov 2022

HAL is a multi-disciplinary open access archive for the deposit and dissemination of scientific research documents, whether they are published or not. The documents may come from teaching and research institutions in France or abroad, or from public or private research centers.

L'archive ouverte pluridisciplinaire **HAL**, est destinée au dépôt et à la diffusion de documents scientifiques de niveau recherche, publiés ou non, émanant des établissements d'enseignement et de recherche français ou étrangers, des laboratoires publics ou privés.



Distributed under a Creative Commons Attribution 4.0 International License

Loss of Energetic Ions Comprising the Ring Current Populations of Jupiter's Middle and Inner Magnetosphere

B. H. Mauk¹ , F. Allegrini^{2,3} , F. Bagenal⁴ , S. J. Bolton² , G. Clark¹ , J. E. P. Connerney^{5,6} , D. J. Gershman⁵ , D. K. Haggerty¹ , V. Hue² , M. Imai⁷ , P. Kollmann¹ , W. S. Kurth⁸ , Q. Nénon⁹ , C. P. Paranicas¹ , A. M. Rymer¹ , H. T. Smith¹ , and A. H. Sulaiman⁸

¹The Johns Hopkins University Applied Physics Laboratory, Laurel, MD, USA, ²Southwest Research Institute, San Antonio, TX, USA, ³Physics and Astronomy Department, University of Texas at San Antonio, San Antonio, TX, USA, ⁴Laboratory for Space and Atmospheric Science, University of Colorado, Boulder, CO, USA, ⁵NASA Goddard Space Flight Center, Greenbelt, MD, USA, ⁶Space Research Corporation, Annapolis, MD, USA, ⁷Department of Electrical Engineering and Information Science, National Institute of Technology, Niihama College, Niihama, Japan, ⁸Department of Physics and Astronomy, University of Iowa, Iowa City, IA, USA, ⁹Institut de Recherche en Astrophysique et Planétologie, CNRS-UPS-CNES, Toulouse, France

Key Points:

- Jupiter ring current energetic ions near and outside Ganymede's orbit are scattered into the loss cone at the strong diffusion limit
- Near the Io and Europa orbits, scattering into the loss cone is very low except within $\sim 60^\circ$ of the downstream positions of the moons
- Near Io's orbit, charge exchange losses dominate over losses from scattering for heavy ions and lower energy ($< \sim 200$ keV) protons

Correspondence to:

B. H. Mauk,
Barry.Mauk@jhuapl.edu

Citation:

Mauk, B. H., Allegrini, F., Bagenal, F., Bolton, S. J., Clark, G., Connerney, J. E. P., et al. (2022). Loss of energetic ions comprising the ring current populations of Jupiter's middle and inner magnetosphere. *Journal of Geophysical Research: Space Physics*, 127, e2022JA030293. <https://doi.org/10.1029/2022JA030293>

Received 14 JAN 2022
Accepted 19 APR 2022

Author Contributions:

Conceptualization: B. H. Mauk
Data curation: J. E. P. Connerney, D. J. Gershman
Formal analysis: B. H. Mauk
Funding acquisition: F. Allegrini, F. Bagenal, S. J. Bolton, J. E. P. Connerney, W. S. Kurth
Investigation: B. H. Mauk, F. Allegrini, F. Bagenal, S. J. Bolton, G. Clark, J. E. P. Connerney, D. J. Gershman, D. K. Haggerty, V. Hue, M. Imai, P. Kollmann, W. S. Kurth, C. P. Paranicas, A. M. Rymer, A. H. Sulaiman
Methodology: B. H. Mauk
Project Administration: S. J. Bolton

Abstract The low-altitude, polar orbit of the Juno mission allows the Jupiter Energetic Particle Detector Instrument to view into, and resolve, the loss cone of energetic ions comprising the low-altitude extension of Jupiter's ring current ions. For regions mapping from just inside Ganymede's orbit to well beyond Ganymede's orbit, energetic ions (>50 keV H^+ and >130 keV Oxygen and Sulfur ions) are strongly scattered into the loss cone and lost to the magnetosphere at the “strong diffusion limit” at essentially all times. We conclude, by arguing against magnetic curvature scattering, that the cause is waves, perhaps associated with Alfvénic variations previously documented in this equatorial region. Scattering is generally weak or nonexistent near the orbits of the moons Europa and Io, except for the regions just downstream of the corotating plasmas. For Io, we sometimes observe moderate, but not saturated, scattering within roughly 60° downstream. Significantly, scattering is weak or nonexistent just upstream of Io's position, an asymmetry echoed in some previous wave observations. A preliminary accounting of the total (longitude-averaged) scattering losses near Io's orbit yields loss rates of order 4%–5% of the strong diffusion limit for H^+ and 5%–7% for heavy ions (O + S). We conclude that near Io's orbit, charge exchange losses likely dominate over scattering losses for heavy ions and for the lower energy H^+ ions (roughly <200 keV).

Plain Language Summary The space environments (magnetospheres) of magnetized planets are populated by energetic charge particles (ionized atoms, or ions, and electrons) encircling the planets. These particles carry a ring-like electric current that distorts the magnetic field away from its nominal “dipole” configuration, familiar from classroom experiments with magnets and iron filings. Here, we examine the loss of these ring current charged particles in Jupiter's middle and inner magnetosphere. The Juno spacecraft, now orbiting Jupiter with a polar, cloud-skimming trajectory allows us, for the first time, to look upward from low altitude and measure the quantity of charged particles that are lost by precipitating onto Jupiter's atmosphere. We find that in the middle magnetosphere, between the orbits of the moons Ganymede and Callisto, the ions are surprisingly lost at the maximum possible rate for precipitation, a rate called the “strong diffusion limit.” In the regions closer to Jupiter, in the vicinity of the moons Europa and Io, the ions are lost from precipitation at a much lower rate. But in addition, the local interactions between these two moons and the space environments close to the moons have profound influences on how fast the ions are being lost due to precipitation.

1. Introduction

At Jupiter, near-equatorial ion populations with energies greater than 50 keV dominate the particle pressures at radial positions greater than about 7 RJ (Mauk et al., 2004; their Figure 5). Also, while Jupiter is known to be largely powered by rotation acting on the plasmas generated in the vicinity of the orbit of Io (~ 5.9 RJ), particle pressure effects are known to play a major role in establishing the global configuration of Jupiter's magnetosphere, and specifically the generation of the canonical magnetodisc configuration (Caudal, 1986; Mauk & Krimigis, 1987; McNutt, 1984; Paranicas et al., 1991). Therefore, the generation, transport, and loss of energetic

© 2022 The Johns Hopkins University Applied Physics Laboratory. This article has been contributed to by US Government employees and their work is in the public domain in the USA. This is an open access article under the terms of the [Creative Commons Attribution License](https://creativecommons.org/licenses/by/4.0/), which permits use, distribution and reproduction in any medium, provided the original work is properly cited.

Software: G. Clark, V. Hue, M. Imai
Writing – original draft: B. H. Mauk
Writing – review & editing: F. Allegrini, F. Bagenal, G. Clark, J. E. P. Connerney, V. Hue, M. Imai, P. Kollmann, Q. Nénon, C. P. Paranicas, A. M. Rymer, H. T. Smith, A. H. Sulaiman

ions, comprising a critical fraction of the ring current populations, are of central importance to understanding the structure and dynamics of Jupiter's magnetosphere.

Here, we address the loss of these energetic particles in Jupiter's inner and middle magnetosphere from about Io's orbit (~ 5.9 RJ) out to well beyond the orbit of Ganymede (~ 15 RJ). By loss, we mean loss from the magnetosphere, although we acknowledge and discuss the fact that modifications in particle energy or pitch angle can look like a loss or source to a particle detector and complicate any analyses. Several processes are thought to contribute (see Jordanova, 2020 for a review of these and other processes as they apply to Earth). One such process is charge exchange between energetic ions and cold neutral gases that are thought to occupy the regions near the orbits of Io (~ 5.9 RJ) and Europa (9.5 RJ; e.g., Brandt et al., 2018; Kirsch et al., 1981; Krimigis et al., 2002; Mauk, Clark, Allegrini, et al., 2020; Mauk, Clark, Gladstone, et al., 2020; Mauk et al., 2003, 2004; Mitchell et al., 2004; Smyth & Marconi, 2003, 2006). An important modification to these earlier considerations is the realization by Smith et al. (2019) that the background agent for the charge exchange can also be low-energy ions in addition to neutral gas, a significant contribution, as we will find, in the vicinity of Io's orbit.

A second hypothesized mechanism of ring current loss is scattering into the loss cone by waves, such as Electromagnetic Ion Cyclotron (EMIC) waves and Alfvén waves (two portions of the same wave dispersion relation). It can be difficult to assess the wave scattering loss mechanisms at measurement positions close to the magnetic equator. The approach that has been generally taken is to combine wave and particle observations with theoretical modeling based on the scattering that the observed waves are likely to engender at Earth (e.g., recent works include: Cao et al., 2016; Liang et al., 2014; Yahnin et al., 2021) and at Jupiter (e.g., Nénon et al., 2018). While Juno observations within the loss cone have previously allowed direct verification in some situations for electrons (e.g., Li et al., 2021 with whistler wave scattering), it is generally not easy to experimentally validate these expectations in novel environments from near-equatorial observations alone. While modern wave interaction tools have become very sophisticated, particularly for Earth applications, such theoretical considerations have sometimes failed in the past in novel environments (e.g., Mauk et al., 1994).

Other possible loss mechanisms include direct absorption by the satellites and scattering by small-scale magnetic structures. For the latter process, scattering can occur as a result of small-scale geometries (small radii of curvature of the field lines) of Jupiter's magnetic configuration near the magnetic equator of the magnetodisc; such scattering is known to occur in the narrow current or “neutral” sheet of Earth's magnetotail (e.g., Sergeev et al., 1983). Quantitative assessment of losses due to direct satellite absorption at Jupiter has a long history, but its role relative to other processes has been uncertain (specifically at Io; e.g., Thomsen et al., 1977). Recent work suggests that satellite absorption can be a narrow perturbation on processes extending over broader regions (e.g., Nénon et al., 2018).

Io's orbital region has been of particular interest. Energetic ion observations there generally show a substantial depletion (e.g., Kollmann et al., 2017; Paranicas et al., 2019). For some ion energies and species, and specifically the higher energy protons, it has been concluded that wave scattering is primarily responsible for these depletions (Nénon et al., 2018; Paranicas et al., 2019). Wave scattering is hypothesized because of wave observations associated with pickup ions, and theoretical considerations associated with the properties of those waves. The evidence of equatorial pitch angle distributions presents a mixed story. Energetic sulfur ions show a substantial depletion near 90° pitch angles, indicative of a role for charge exchange losses near the equator due to the presence of neutral gases there (Lagg et al., 1998; Mauk et al., 1998; Nénon & André, 2019; Williams et al., 1996). However, published proton distributions (although incomplete) do not appear to show this depletion (Mauk et al., 2004).

The Juno mission has provided a unique opportunity. Juno flies at low altitudes over the polar regions such that it is able to resolve the loss cones of the high-latitude extensions of the ring current populations. These observations are available for regions that map magnetically from well outside of Ganymede's region and in to Io's region. Here, we examine and analyze the differences between the structure of the energetic ion loss cones for the downward and upward directions. We use this information to estimate the scattering loss rates for these energetic ions, specifically for the Io regions. Along the way, we investigate the possible sources and locations of the scattering. Near Io, we specifically compare the derived loss rates with those engendered by charge exchange losses.

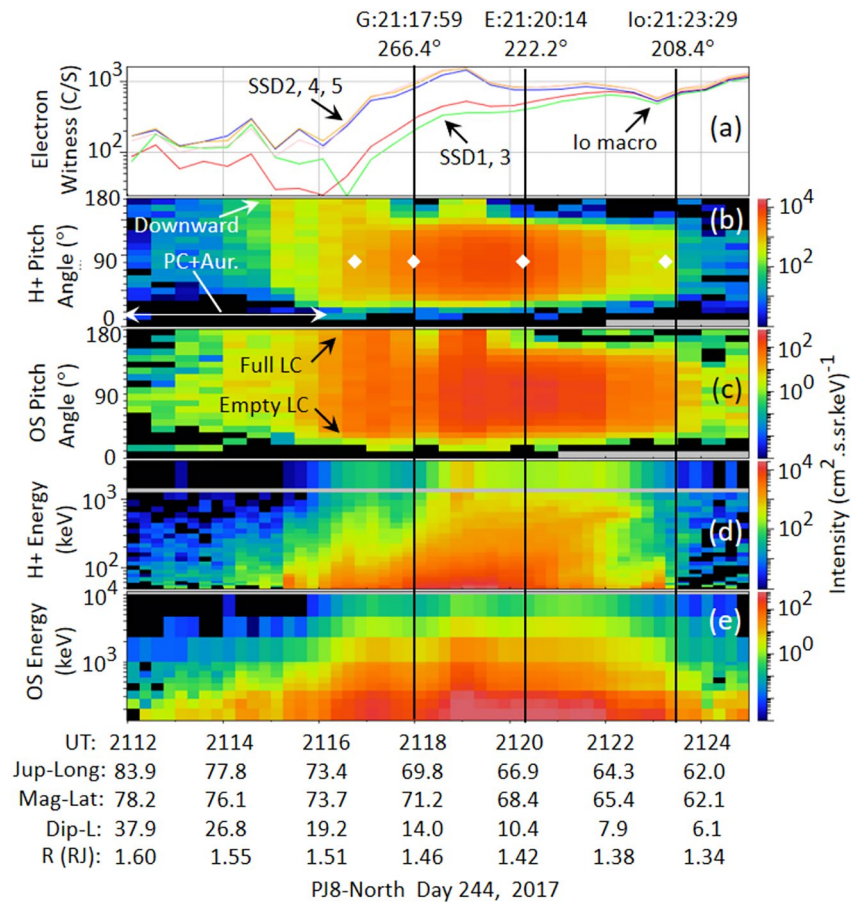


Figure 1. Ion (H^+ and oxygen and sulfur ions designated OS) and some electron data from the Juno Jupiter Energetic Particle Detector Instrument (JEDI) at low altitudes over Jupiter during the northern hemisphere portion of Juno perijove 8 (PJ8-N). Additional details of the following explanations are provided in the text. (a) Electron data from the JEDI “witness” detectors. (b) H^+ pitch angle distribution spectrogram averaged over the proton energy channels of JEDI (50–4,000 keV). (c) Oxygen plus sulfur (OS) ion pitch angle distributions averaged over the energy channels of JEDI (130–10,000 keV). (d) H^+ energy distributions averaged over pitch angle. (e) Heavy ion (OS) energy distributions averaged over pitch angle. The x axis shows both time and various parameters related to the position of Juno. The white diamonds within Panel (b) show the times of the individual pitch angle samples shown in Figure 2. The vertical black lines show when Juno crossed the magnetically mapped positions of the plasma tails of the moons Ganymede, Europa, and Io (see text for additional details). The labels on the vertical black lines show the downstream azimuth position of the Juno crossing point relative to the azimuthal position of each moon. For this period of time, Io and Europa are far away in azimuth from the Juno satellite crossing positions.

2. Juno Data

Figures 1 and 2 show the nature of the ring current ion data that is the subject of this study. These panels show data obtained by the Jupiter Energetic Ion Detector Instrument (JEDI) on the polar orbiting, atmosphere-skimming Juno spacecraft now orbiting Jupiter. The Juno mission is described by Bolton et al. (2017) and the JEDI instrument is described by Mauk, Haggerty, Jaskulek, et al. (2017). The magnetometer instrument on Juno (Connerney et al., 2017) allows for the determination of the pitch angles of the particles measured by JEDI; pitch angle is the angle between the particle velocity vectors and the magnetic field direction.

The Juno spacecraft was launched in 2011 and was inserted into Jupiter orbit in July of 2016, ultimately with the following orbit parameters: 1.05×112 RJ polar ($\sim 90^\circ$ inclination), ~ 53.5 day period elliptical orbit with the line-of-apsides close to the dawn equatorial meridian. Following insertion, the line-of-apsides has been slowly precessing southward ($\sim 1^\circ$ per orbit) and toward the nightside ($\sim 4^\circ$ per orbit). Figure 2 in Zhang et al. (2020) provides a good sense regarding how the orbit evolves over time. JEDI measures energy, angle, and composition distributions of electrons (~ 25 – $\sim 1,200$ keV) and ions (protons: ~ 10 keV to > 4 MeV; oxygen and sulfur from

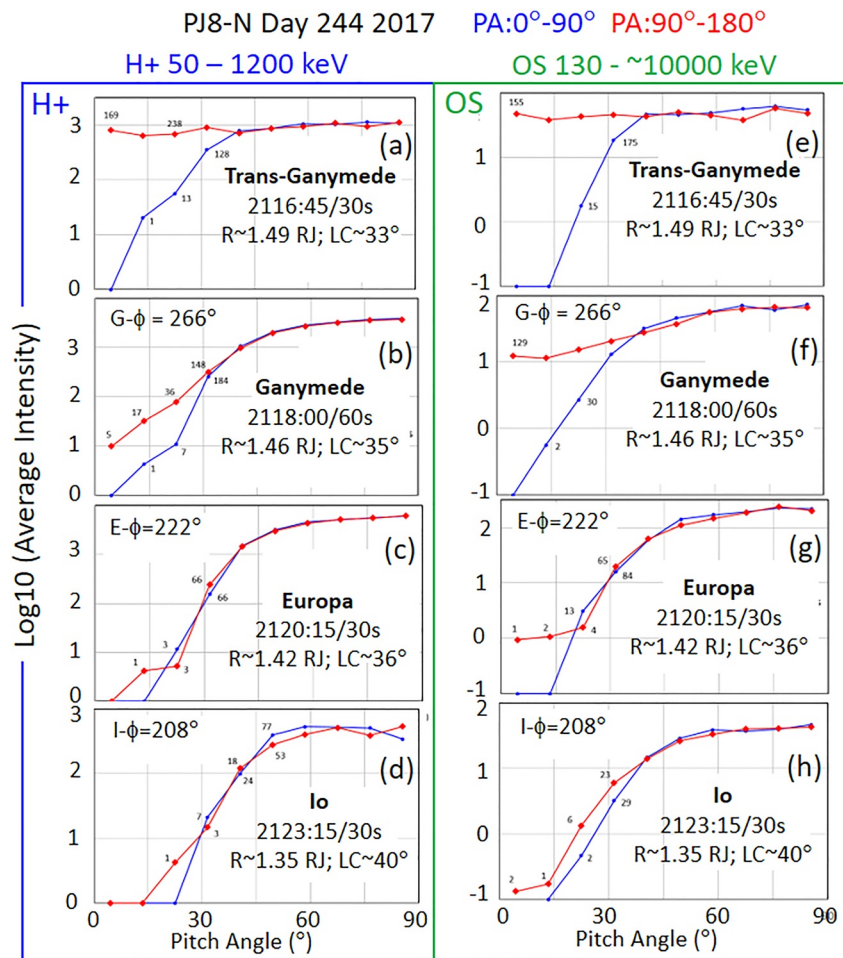


Figure 2. H^+ (left column) and heavy ion (OS; right column) individual pitch angle distributions obtained at four different selected times during the time period shown in Figure 1. The units on the intensity values are $1/(\text{cm}^2 \text{ s sr})$. The four times are shown in Panel (b) of Figure 1 using white diamonds. The four times correspond to positions that magnetically map to a region outside of Ganymede (trans-Ganymede; panels (a) and (e)), near-Ganymede (panels (b) and (f)), near-Europa (panels (c) and (g)), and near-Io (panels (d) and (h)). The upgoing and downgoing pitch angles are folded on top of each other by modifying the pitch angles of one or the other of these pitch angles using: $PA' = 180 - PA$, where PA is pitch angle. The top line of the figure shows which range of pitch angles correspond to which distribution color. In all cases, red distributions are downward and blue distributions are upward. For the 3 lower panels in each column, the azimuth position of the relevant moon is provided. Also, in all panels, the radial position of the measurement is provided and the corresponding estimated loss cone size (LC) based on the formula provided in Mauk, Haggerty, Paranicas, et al. (2017).

~ 130 keV to >10 MeV). Mauk, Allegrini, et al. (2020) provide an overview of the findings of the JEDI investigation over Jupiter's polar regions, and Allegrini, Mauk, et al. (2020) show JEDI data in the context of the lower energy plasma data (from the JADE instrument).

Figures 1 and 2 are representative of a number of other figures that we show in this paper. We therefore focus on describing their various features. Figure 1 shows both energetic ion, and some electron, data obtain during the northern portion of Juno's perijove 8 (PJ8-N). The horizontal axis shows the changing position of Juno, and in particular, shows the low-altitude position ranging between about 1.6 and 1.3 Jupiter radii (1 RJ = 71,492 km). Here, JEDI, with its Full-Width and Half Maximum (FWHM) angular resolution of about $9^\circ \times 17^\circ$ (see more below), is at a low enough altitude to resolve the pitch angle loss cone, the cone of ion trajectories that just barely graze the atmosphere where the particles are lost.

The equatorial positions that magnetically map from Juno's position are best evaluated using the vertical black lines in Figure 1. They show the predicted positions of the instantaneous plasma tails of the moons Ganymede

(near 15 RJ at the equator), Europa (near 9.4 RJ), and Io (near 5.9 RJ). These positions were calculated using the JRM09 internal magnetic field model derived from Juno data (Connerney et al., 2018) together with the contributions of external currents in the form of the magnetodisc currents of Connerney et al. (1981). The magnetodisc and external currents have now been updated by Connerney et al. (2020) and Pensionerov et al. (2019, 2021). However, those updates are not utilized here as achieving the “exact” calculated mapping is judged to be not critical to the present discussions. The calculations used here were performed by one of us (VH) using tools developed by another (MI; see Acknowledgments for the site where these calculations are documented). The labels on each of the vertical black lines show how far around Jupiter, in the direction opposite to the plasma flow, these moons resided at the time that Juno crossed these positions. It is important to recognize that the instantaneous positions of the tails of the moons can be a little different from the time-averaged influence that the moons have on the environment. Notice, for example, in the right-hand side of the top panel (a) of electron data, the presence of a “macro-signature” of the moon Io that is slightly displaced from the instantaneous position of Io's tail. That macro-signature is the signature of time-averaged absorption of the energetic electrons by the moon or by other processes associated closely with the moon. Very energetic protons will also show a macro-signature, but we believe that the one shown in Figure 1a is within the penetrating >10–15 MeV electrons (as discussed in the next paragraph).

The top panel of Figure 1 (designated here as Figure 1a) shows total electron rates sampled by what are called the “witness” detectors on JEDI (Mauk, Haggerty, Jaskulek, et al., 2017). These detectors are designed to sense the condition whereby the electron sensors are overwhelmed by electrons with sufficient energy to penetrate the side walls of JEDI (>10–15 MeV). Solid-State-Detector (SSD) units 2, 4, and 5 (as labeled in the figure) are bare detectors that measure foreground electrons with energies >25 keV (and >~50 keV protons if their intensities are competitive). SSD1 and SSD3 have shields over them such that they measure foreground electrons with energies >0.5 MeV. When high-contrast angular structure is not present, these two clusters of measurements pinch together when the rates are overwhelmed by electron penetrators as they do on the right side of Panel (a). The ion data shown in the other panels are obtained by a coincidence system that substantially filters out the consequence of penetrating electrons. However, when the electron witness detector responses are pinched together, and the rates rise substantially above 10^3 counts per second, the ions can suffer contamination from what are termed “accidental” events, whereby different electrons simultaneously stimulate the multiple signal elements of the ion measurements. In Figure 1a, the fact that the electron rates rise only to about 10^3 tells us that the ion data are relatively clean of contamination, at least relative to the robust foreground counts.

Figures 1b and 1c show, respectively, proton (H^+) and heavy ion (OS) pitch angle distributions of the energy-channel-averaged intensities. The intensities are averaged over the range of energy channels shown in the energy spectrograms in Figures 1d and 1e for H^+ and OS ions, respectively. The heavy ions are a mix of Oxygen (O) and Sulfur (S). At energies below about 600 keV, JEDI does not resolve O and S. The channels at these lower energies are a mix of these two species. At higher energies, JEDI has separate channels for O and S, but for this study, we continue to mix together these two species. We use the label “OS” to designate this mix. Note that the energy spectra (Figures 1d and 1e) can show dispersed signatures that have been attributed to dynamic injections (Haggerty et al., 2019). The dispersion sense of these injections depends on the age the injections and the rapidity of the radial motion of the spacecraft as described in the context of Saturn injections by Mauk et al. (2005).

JEDI measures the pitch angle distributions in a somewhat unusual fashion for energetic particles. JEDI consists of three independent instruments, each of which has 6 telescopes arranged in an $\sim 160^\circ$ fan. Ions are measured only with two of the sensors, JEDI-90 (J90) and JEDI-270 (J270). These sensors are oriented to create a field of view of approximately 360° within a plane roughly perpendicular to the spacecraft spin vector. With this configuration, JEDI provides a roughly complete pitch angle distribution at every instant of time, provided the magnetic field is roughly contained within the view plane of the sensors. The FWHM resolution of JEDI is roughly $9^\circ \times 17^\circ$ with the 17° dimension oriented along the 160° fan. In high-resolution mode, JEDI accumulates for 0.25 s at a cadence of 0.5 s (ions and electron measurements are sub-commutated). Hence, given the 30-s spin period of Juno, the field of view is rotated by 3° during an accumulation. The 12 different telescopes within the view plane oversample any structures by cutting through them with different rotational phasing with respect to the structures as the sensor accumulates over 3° intervals every 6° . Therefore, any structures within the angular distribution are smoothed over (convolved with JEDI's field of view) during the time of a 30 s spacecraft spin. The resulting measured angular distributions are very stable and reproducible despite the relatively large resolution

element ($\sim 17^\circ$) in the direction of rotation. We note, however, that the 160° fans of these two instruments do not reside exactly perpendicular to the spin axis; their orientations are tilted and twisted by up to 10° to avoid viewing the huge Juno solar panels. In all of the data plots that we show here, the sample time is usually 30 s or one spin period. However, sometimes, to either reveal additional structure or to increase the statistical counts that go into the sample, we use 15 s or 60 s, respectively.

Figure 2 shows individual samples of the pitch angle distributions at four different times. Time runs from top to bottom or from bottom to top, depending on whether Juno is in the northern or southern hemisphere. In all cases for the present study, the top to bottom samples correspond to a region beyond Ganymede (trans-Ganymede), near Ganymede, near Europa, and then near Io. The sample times are displayed in Figure 1b using white diamonds overlaying the colored pitch angle distributions. In Figure 2 and in subsequent similar figures, proton (H^+) distributions are shown on the left, and heavy ion (OS) distributions are shown on the right. To reveal the differences between upgoing and downgoing loss cones, we have folded these two pitch angle measurements on top of each other. In all of our plots, the downgoing distributions are shown with red diamonds with red connecting lines. In Figure 2, the downgoing pitch angles depicted in red have been calculated using: $PA' = 180^\circ - PA$, where PA is the actual measured pitch angle and PA' is the derived pitch angle. We note finally that JEDI particle counts are somewhat limited when measuring these projections of the ring current populations. In the loss cone regions, individual points are labeled with the number of counts that went into the calculation of the average intensities. Measurements with zero counts are positioned on the x axis. We chose 9° bins for the pitch angle displays because of the limitations in counts. Because of the oversampling that JEDI accomplishes, we may choose any one of a broad range of pitch angle bin sizes.

Because JEDI is somewhat count limited with these measurements, we have chosen to avoid parsing the measurements in this paper to obtain an energy dependence on the pitch angle structures for this study. Our preliminary attempts to obtain an energy dependence did not show any significant differences. However, the relatively low count rates mean that this conclusion has a substantial error associated with it.

Each panel of Figure 2 is labeled with the radial position of Juno at the time of the measurement, and an estimate of the loss cone size calculated using the simple expression given by Mauk, Haggerty, Paranicas, et al. (2017). In comparing upgoing with downgoing distributions, we desire to use those pitch angles that are inside the loss cone. Because of the smoothing effect of the finite size of JEDI's field of view, we add about 8° to the loss cone value as our starting point for calculating differences (see later discussions). For example, in Figure 2e, we see that the calculated loss cone is about 33° . However, it is a pitch angle value of about 40° where the upgoing and downgoing intensities come together. We use the bin closest to $LC + 8^\circ$ as a starting point for comparisons.

We note finally that the regions outside of Ganymede's orbit are the regions thought to map to Jupiter's main auroral regions. However, based on our extensive experience with the JEDI data, we are able to cleanly separate auroral acceleration processes from the measurement of ring current populations (Mauk, Allegrini, et al., 2020). In Figure 1b, a double arrow on the left shows where the electron data (not shown) show clear evidence of acceleration associated with Jupiter's nondiffuse main aurora or polar cap and specifically, where we observe upward going electron angle beams closely aligned with the magnetic field (again see Mauk, Allegrini, et al., 2020). Often there is direct evidence of auroral acceleration within the ion plots that we are showing. Such direct evidence will be noted when discussing other examples. Equatorward of these regions of auroral electron acceleration is the regions of diffuse aurora resulting from the scattering of trapped electrons into the loss cone (e.g., Li et al., 2021; Mauk, Allegrini, et al., 2020). The regions that we study here with regard to ions include all of the regions that have been designated as the diffuse auroral regions. It is useful to compare these transitions with the Galileo spacecraft observation of electron behavior near the equator. Specifically, Tomás et al. (2004) observed a radial transition in electron pitch angle distributions from bidirectional to trapped distributions as one moved inward across a boundary that ranges from 17 to 10 RJ. The anisotropy is very modest (see also Mauk & Saur, 2007), however, and the role of radial transport in redistributing the locations of these transitions is unknown. For example, Bhattacharya et al. (2001) argue that the energy flux associated with the bi-directional electron distributions is sufficient only to power the diffuse aurora. These bidirectional distributions appear not necessarily to have been freshly generated. We note that the "witness" electron measurements (Figure 1a) generally do not easily reveal auroral acceleration processes because those sensors typically do not view along the magnetic field lines.

3. Juno Observations

3.1. Perijoves With Only Distant Moons

For this study, the most significant findings relate to the symmetry or lack of symmetry between the upgoing and downgoing loss cones. In Figures 1b and 1c, we see that over a substantial fraction of the time period shown, and specifically outside of Europa's position, the downward loss cones (top portions of the panels) are full, whereas the upward loss cones are relatively empty. This condition, however, is not sustained as we move into the regions of first Europa and then Io.

These general findings are better quantified in Figure 2. Here, we find that the “trans-Ganymede” pitch angle distributions show, not just “full” loss cones, but classically full at what would be very close to the strong diffusion limit. Within the range of pitch angles sampled by JEDI, the downward pitch angles are as flat as JEDI can determine. This condition is generally characteristic of all ring current samplings that we have studied in sub-auroral, trans-Ganymede regions. These ions (both H^+ and OS) appear to be scattered at such a rate that they completely fill the loss cone within a single bounce of the ions between hemispheres. This condition would be the classic definition of scattering at the “strong diffusion limit” (e.g., Lyons & Williams, 1984). At this limit, it is easy to calculate the lifetime of these particles as we will discuss in a later section.

As we move inward from Ganymede, we see a decrease in the scattering in the vicinity of Ganymede (Figures 1b, 1c, 2b and 2f) and then a restoration of fairly strong scattering between Ganymede and Europa (Figures 1b and 1c). The strong scattering often extends to regions between Ganymede and Europa, but a dip in that behavior just at Ganymede is not always observed. We offer no explanation for the dip near Ganymede for this case.

As we move inward to Europa and Io, the level of scattering becomes very low. In later sections, we present a scheme to quantify the level of scattering. We note that this level of scattering, or the complete absence of any level of scattering, is typical for the Europa and Io regions when the positions of the moons are far from the measuring positions. In Figures 2c and 2g, we see that Europa was 222° upstream of the measurement position (see the label $E-\phi = 222^\circ$). In Figures 2d and 2h, we see that Io was 208° upstream of the measurement position. At both Europa and Io, we see small amounts of apparent scattering. We find that these logarithmic plots can be misleading in suggesting more scattering than is revealed quantitatively. Specifically, it is comparisons closer to the edge of the loss cones that tend to dominate the quantitative assessments of scattering rates that we reveal in a later section.

More perijoves with conditions like those shown in Figure 1 (with relatively distant moons) are shown in the Appendix for PJ8-S and PJ1-N (Figures A1-A, A1-B, A2-A and A2-B, respectively). We have chosen to put a number of different examples in the Appendix in order not to overwhelm the reader and diffuse the discussions. We have chosen an Appendix rather than a Supporting Information section in order to make these very important examples part of the citable record. Figure A1 (PJ8-S) shows several explicit examples of ion auroral acceleration just beyond the Ganymede regions and illustrates the broad strong scattering precipitation regions extending closer to the Europa regions than was apparent in Figure 1. Figure A2 (PJ1-N) shows auroral acceleration overlapping the trans-Ganymede regions to a greater degree, making the Ganymede and trans-Ganymede regions a little less clear.

3.2. Perijoves With Nearby Upstream Moons

Figure 3 shows an example (from perijove PJ5-N) of a crossing of the low-altitude extensions of the ring current for the conditions where the mapped positions of the moons Io and Europa are much closer to the Juno crossing position. The labels for the vertical lines for Europa and Io show that these two moons were upstream of the Juno crossing positions by only 7.1° and 6.7° , respectively. These pitch angle distributions (Panels 3b and 3c) show distinct signatures associated with Io, and we believe Europa.

Figure 3 shows somewhat messier conditions than Figure 1 for a couple of reasons. The geometry of this encounter was such that the region was crossed at a rate that was almost twice as fast as what occurred in Figure 1. In Figure 1, Juno transited from the Ganymede crossing to the Io crossing in about 5.5 min. In Figure 3, that crossing occurred in only about 3 min. As a result, we utilized accumulations of 15 s (1/2 of a spin) rather than

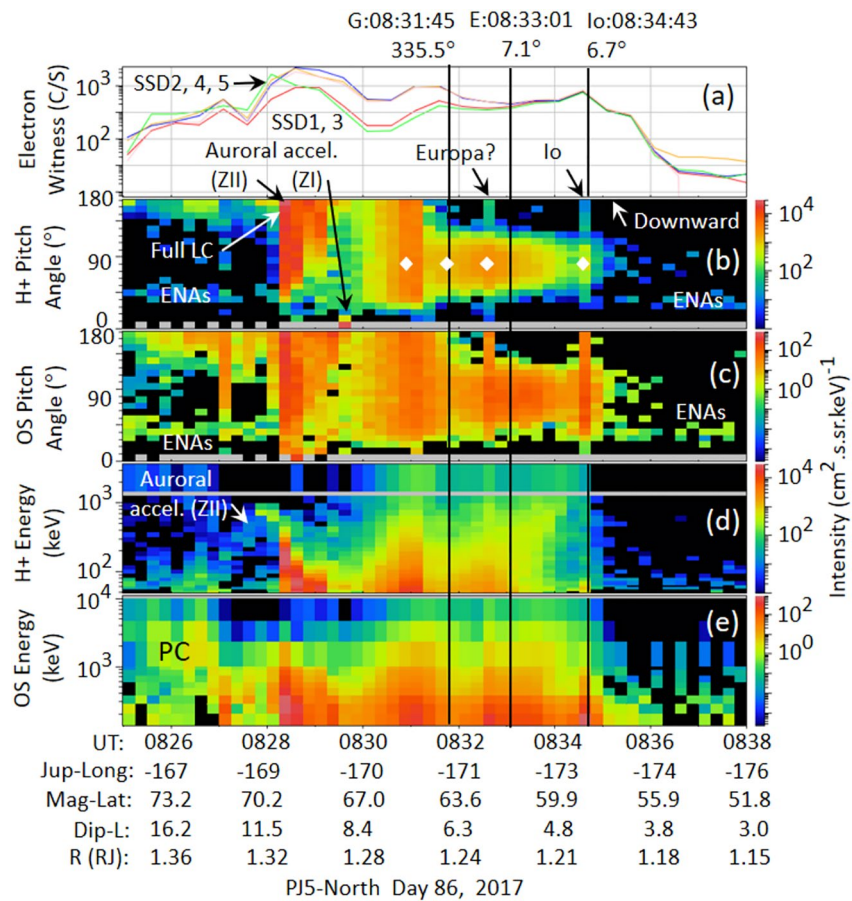


Figure 3. Same as Figure 1 except the time period is for the northern portion of Juno perijove 5 (PJ5-N). For this period of time, Io and Europa are close in azimuth in the upstream direction from the Juno satellite-crossing positions.

the usual 30s for Figure 3. Note that for all of the encounters examined for this study, we always generate plots with multiple accumulation periods to make sure that there is no hidden structure averaged away by the chosen accumulation period. For Figure 3, the shorter accumulation period was required to reveal the narrowness of the distinct responses near Europa and Io.

The period shown in Figure 3 also reveals much more activity associated with Jupiter's auroral acceleration processes. The regions that we study here occur equatorward of these auroral acceleration regions and generally coincident with the trapped electron populations that are associated with the diffuse aurora. We spend some time here discussing the auroral features in Figure 3 to make it clear that the ring current features that are the focus of the present study are distinct from the auroral acceleration processes. Mauk, Allegrini, et al. (2020) have revealed two distinct regions of main auroral acceleration (in addition to the diffuse aurora), both of which result in intense auroral emissions. Zone I, just poleward of the diffuse aurora, is a region of downward electron acceleration (sometimes broadband and sometimes electrostatic) and is where magnetic field-aligned electric currents are thought to be upward (as proven by one distinct example in this cited paper). Often associated with this region is the upward acceleration of ion beams. Such a beam is seen Figure 3b and is labeled “ZI” for Zone I. Generally, poleward of Zone I is a region of bidirectional, broadband electron acceleration, thought to be associated with downward electric currents (again as verified for one distinct event). Sometimes (but not always), this region is associated with downward ion inverted-V’s (downward electrostatic potentials) and intense proton distributions with broad angular distributions. We see just such a distribution in Panels 3b and 3d, labeled “ZII” for Zone II. An additional feature of interest is labeled “PC” for “polar cap” on the left side of Panel 3e. Here, as first documented by Clark et al. (2017), and studied more extensively by Clark, Mauk, Kollmann, Paranicas et al. (2020) and Mauk, Allegrini et al. (2020), we see a downward heavy ion inverted-V structure with energies

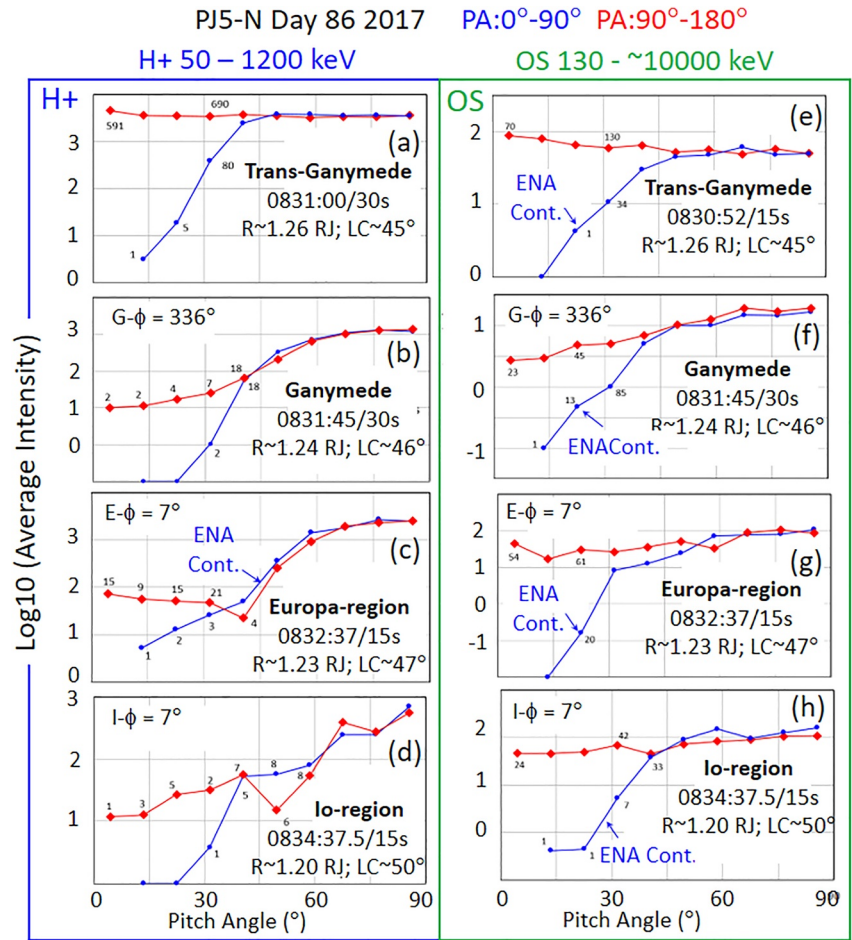


Figure 4. Same as Figure 2 except that it refers to time periods in Figure 3.

up to about 2 MeV, corresponding to downward electrostatic potentials here of up to 2 MV. Note that all of the features identified here are more distinct when the energy plots are generated with pitch angle filters that focus on the field-aligned directions.

There is one additional feature in Figures 3b and 3c that is important because it can contaminate the pitch angle structures that we are trying to characterize. That broad feature is labeled “ENAs” on the left and right portions of Panels 3b and 3c. These features were studied extensively in Mauk, Clark, Gladstone, et al. (2020) and represent Energetic Neutral Atoms that are generated when nearly precipitating ions interact with Jupiter’s upper atmosphere. They are thought to be the result of precipitation by the ion feature labeled “Auroral Acceleration (ZII)” in Figure 3b. However, we now realize that the ring current precipitation outside of Ganymede could be contributing. While these ENA detections are sparse, their intensities can become comparable to the very low ion intensities near the bottoms of ion loss cones. In Figure 4, we have added labels “ENA Cont,” where we think the ENA emissions are slightly contaminating the upward ion pitch angle distributions.

Once again (Panels 3b, 3c, 4a, and 4e), the trans-Ganymede ring current regions are precipitating at the strong diffusion limit. We attribute the slight rise in the intensities in Panels 4a and 4e as one looks to the very lowest pitch angles as being due to spatial gradients that reveal themselves as we traverse the regions too quickly.

The big difference between Figures 3 and 1 is that in Figure 3, the moons Europa and Io are nearby and upstream. There we see relatively strong scattering into the loss cones near Europa and near Io. The apparent Europa signature is somewhat displaced from where it is expected; such displacements in lower energy plasma data are observed in the vicinity of other near-Europa crossings (Allegrini, Gladstone, et al., 2020). The heavy ion

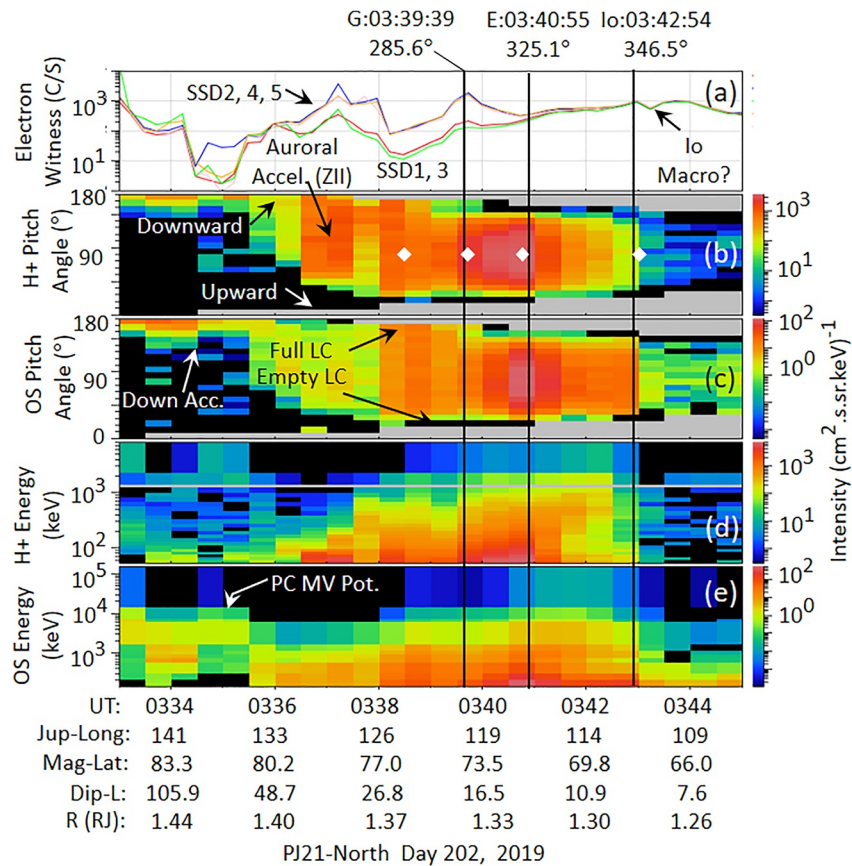


Figure 5. Same as Figure 1 except the time period is for the northern portion of Juno perijove 21 (PJ21-N). For this period of time, Io is close but downstream in azimuth from the Juno satellite-crossing position.

scattering (Panels 4g for Europa and 4h for Io) appears to approach the strong scattering limit for the very narrow regions (Panels 3b and 3c) around these near-moon encounters. We note that for this PJ5-N encounter, there is more going on than just scattering into the loss cone. Whatever has caused the apparent scattering near Io (and near Europa as well) appears to have accelerated the ions as well. That interpretation is based on the overall brightening of the intensities at all pitch angles relative to adjacent intensities. This conclusion reminds us of the work of Clark, Mauk, Kollmann, Szalay, et al. (2020) where, for a particularly close encounter with the footpoint of Io, strong ion conic acceleration was observed and attributed to the action of observed Alfvén and/or electromagnetic ion cyclotron (EMIC) wave acceleration.

Two other perijove passes with nearby moons (PJ5-S and PJ22-N) are examined in the Appendix (Figures A3 and A4, respectively). In Figure A3 (PJ5-S), there is some “accidentals” contamination at the lowest L (left side) because of the high values of the electron witness detectors. The proton (H⁺) scattering near Io looks more like a scattering process without the obvious energization. Again, the apparent Europa signature is somewhat displaced from the expected positions. In Figure A4, it is only Io that was close to (and upstream of) the Juno crossing position. However, Europa is even closer, but in the downstream regions, no strong scattering appears to be associated with Europa.

3.3. Perijoves With Nearby Downstream Moons

Figures 5 and 6 shows a final example (for perijove PJ21-N) where the spacecraft was relatively close to the Io flux tube, but in the upstream direction (about 13.5°). As with the case of Europa shown in Figure A4 and mentioned in the last paragraph, we believe that it is significant that no strong scattering is observed in the vicinity of Io’s L-shell crossing. An even more convincing case can be seen in the Appendix in Figure A5 for perijove

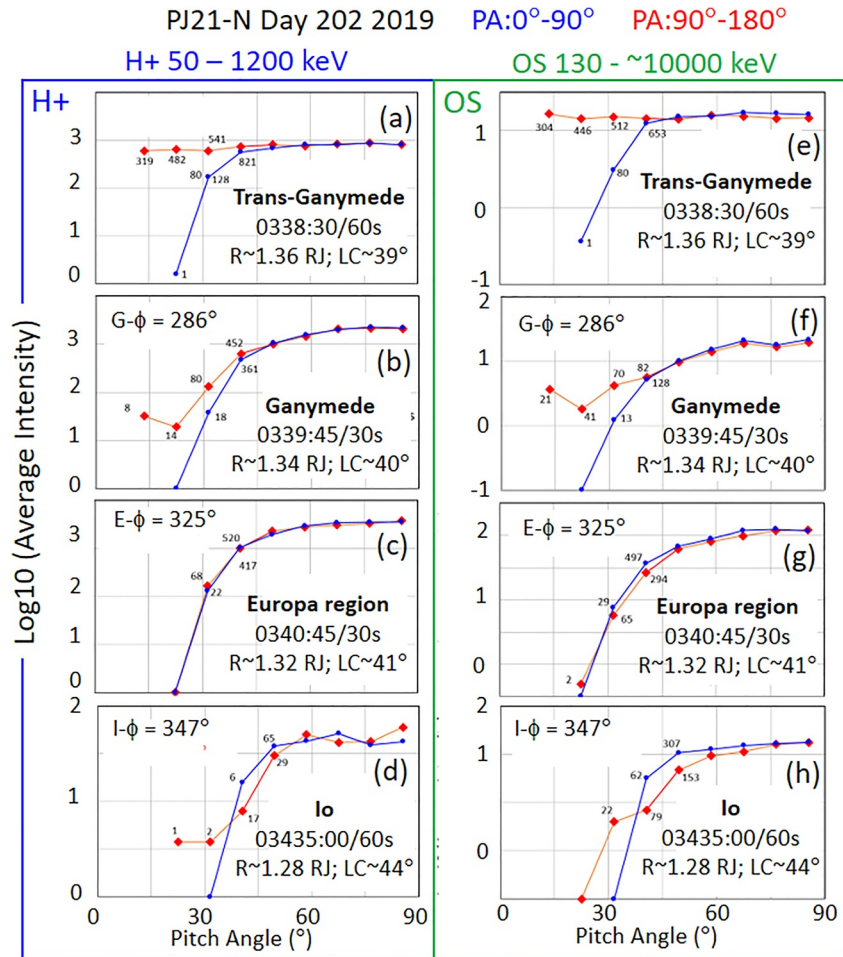


Figure 6. Same as Figure 2 except that it refers to time periods in Figure 5.

PJ13-S. Here, Io is just 6° downstream of the Juno crossing point. We have not provided a complete set of plots for this example because overall the pitch angle sampling is so poor. However, in the vicinity of Io, it is clear that there is no strong scattering into the downward loss cone (as the lower portions of the two pitch angle plots show).

4. Analyses

4.1. What Causes Strong Scattering in the Trans-Ganymede Region?

Our first hypothesis regarding the cause of the scattering in the trans-Ganymede and near Ganymede regions is that the ions are scattered by the tight geometries (small radii of curvature) of the magnetic field lines close to the magnetic equator, given the presence of the magnetodisc configuration. Such scattering is known to occur at Earth as one moves into the tight geometries within Earth's magnetotail (e.g., Sergeev et al., 1983). Scattering by the small radii of curvature of magnetic configurations has been studied theoretically (e.g., Büchner & Zelenyi, 1989; Sergeev et al., 1983) and has been tested with satellite data (e.g., Lavraud et al., 2016). Scattering and nonadiabatic behaviors of ions near Jupiter's neutral sheet have been examined theoretically by Birmingham (1982) and Selesnick et al. (2001). Theorists define the parameter $\kappa^2 \equiv r_c/\rho$, where ρ is the maximum gyroradius of the particle along the field line (e.g., at the magnetic equator) and r_c is the minimum radius of curvature of the magnetic field line (also at the magnetic equator for our application). Simulations and observations (Büchner & Zelenyi, 1989; Lavraud et al., 2016; Sergeev et al., 1983) have shown that some scattering begins weakly when κ^2 is just below 25, but strong scattering occurs with κ^2 is less than about 11.

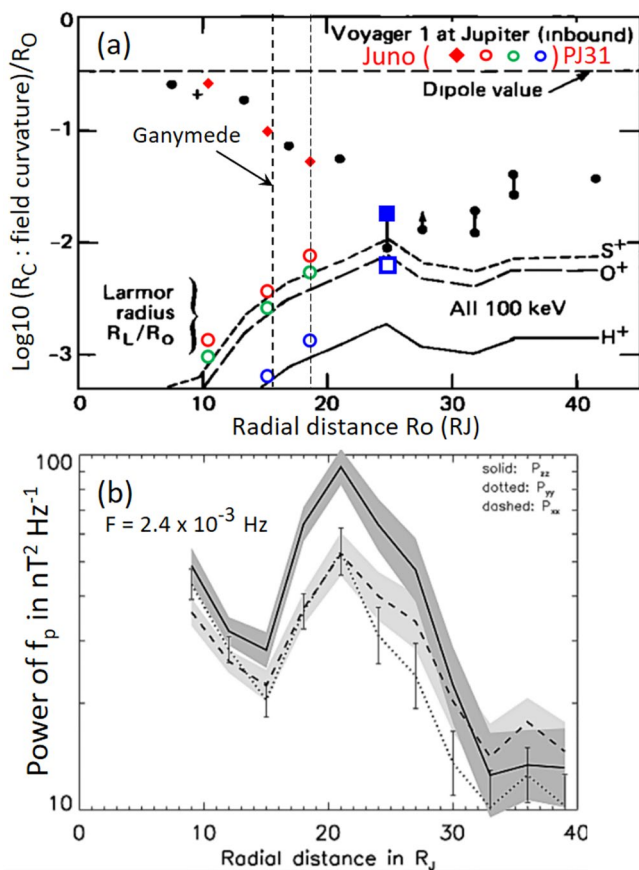


Figure 7. (a) Equatorial radius of curvature of Jupiter's magnetic field configuration as a function of radial position normalized by radial position, and the normalized size of the ion gyroradii at the minimum magnetic field position for 100 keV H^+ , O^+ , and S^+ . The black points and curves were determined by Mauk and Krimigis (1987) using dayside Voyager-1 data, the colored diamonds and circles were determined using the Juno magnetometer data during the nightside perijove 31 (PJ31) using the procedures developed in Mauk and Krimigis (1987), and the blue squares are from an analysis of the statistical results of Liu et al. (2021) for the nightside (see text). (b) Alfvénic magnetic turbulence as measured by Galileo and reported by Saur et al. (2003) at a reference frequency of 2.4×10^{-3} Hz.

The minimum radius of curvature of Jupiter's magnetic field has been estimated observationally. Figure 7 shows with black symbols the estimates provided by Mauk & Krimigis (1987) for the Voyager 1 dayside encounter with Jupiter. The red and filled diamonds show estimates using Juno magnetometer data for the nightside perijove PJ31 using the procedure developed by Mauk & Krimigis (1987). Only late Juno orbits can be used for this procedure because early orbits did not cross the magnetic equator in the region of interest. Juno results show substantial consistency with the Voyager results. It is likely true that the dayside Voyager results are not representative of the situation beyond 20 RJ in general for all local times. Liu et al. (2021) have performed a statistical analysis of current sheet thickness and magnetic field strengths using Juno data beyond 20 RJ for the nightside. Using the characteristic values for the most planetward statistical bin centered on 25 RJ from their work, we have positioned a dark blue-filled square based on numbers from that work. We used mean numbers from Figures 2 and 3 from Liu et al. (2021) and calculated a minimum radius of curvature (~ 0.46 RJ) using the Harris sheet formulation used by those authors. Also shown in Figure 7a are the maximum gyroradii for 100 keV H^+ , O^+ , and S^+ . We show the Voyager results (in black lines), the Juno PJ31 results using colored open circles, and the Liu et al. (2021) number with an open blue square. For the regions planetward of 20 RJ, rough consistency is seen between the Voyager (dayside) and Juno (nightside) results. For the Liu et al. (2021) results beyond 20 RJ, we see a weaker magnetic field strength for the center of the neutral sheet for the nightside than Voyager found for the dayside.

Right at Ganymede (shown with a vertical dashed line), the κ^2 for 100 keV H^+ , O^+ , and S^+ is roughly 300, 50, and 30. At 18.8 RJ (the point of the outermost Juno PJ31 results), these same values are roughly 83, 16, and 10. One might try to make a case for neutral sheet scattering of the heavy ions, particularly for those with energies higher than 100 keV (although for sulfur, the typical charge state is thought to be 2 or greater, decreasing the size of the gyroradius; Clark et al., 2016). However, it would appear unlikely that neutral sheet scattering can explain the fast (single bounce) isotropization of the protons at the 18.8 RJ position and planetward. Beyond 20 RJ, the strong scattering by magnetic curvature clearly becomes much more important for H^+ .

A second hypothesis is that Alfvén or EMIC waves scatter the ions into the loss cone. Some evidence for such waves was provided by Saur et al. (2003) who showed a distribution of Alfvénic variations rising dramatically just outside of Ganymede's orbit (Figure 7b). These authors hypothesized that

the wave distribution represents a turbulence that is a key link in the chain of processes that power Jupiter's main aurora. That hypothesis (see also Saur et al., 2018) remains viable given the fact that the brightest aurora at Jupiter is caused by broadband electrons (with monotonically falling distributions rather than the peaked distributions associated with electrostatically acceleration; Allegrini et al., 2017; Mauk, Haggerty, Paranicas, et al., 2017). However, for the present study, the mere presence of such a distribution of variations is highly suggestive that the region is active in the generation of waves, and that some component of such waves might provide a scattering mechanism for the trans- and near-Ganymede H^+ and OS ion populations. The high-frequency end of the Alfvén/Ion-Cyclotron wave dispersion curve is known to scatter ions (e.g., Cao et al., 2016; Liang et al., 2014; Yahnin et al., 2021), and perhaps Alfvén waves that are kinetic, with perpendicular wavelengths comparable to ion gyroradii, could play a role. However, it is beyond the scope of the present study to discuss the mechanism of such scattering and to expand the characterization of the frequency structures of the observed wave distributions. While EMIC waves have been observed at Jupiter inside perhaps $L = 13$ RJ (Lin et al., 1993), we have found no published record of EMIC waves in the trans-Ganymede region.

4.2. How Fast Are the Loss Rates Caused by Scattering?

At the strong scattering or diffusion limit, it is straight forward to calculate ion loss rates. One assumes that the loss cone is completely full, and that the speed at which the ions in the loss cone are lost is approximately $\frac{1}{2}$ the bounce period of the respective ions. Assuming small loss cones, Lyons and Williams (1984) provide the following formula for the e-folding loss times:

$$T_{sd} = \frac{4LR_p}{2.2V \sin^2(\alpha_{lc})} \quad (1)$$

where T_{sd} is the “strong diffusion” e-folding time, L is the magnetospheric distance parameter in units of the planetary radius (R_p), V is the particle speed, and α_{lc} is the equatorial loss cone size. $\sin^2[\alpha_{lc}]$ is B_{eq}/B_{atm} , where B_{eq} is the field strength at the magnetic equator, and B_{atm} is the strength at the top of the atmosphere where the ions are stopped or removed. Given the high degree of structure in Jupiter's internal magnetic field (Connerney et al., 2018), there is a range of magnetic field strengths where ions might precipitate. Choosing median values, and estimating equatorial field strengths from Connerney et al. (1981), we find the following for four different positions in Jupiter's equatorial magnetosphere and for 100 keV H^+ and OS ions:

$R(RJ)$:	20	15	9.4	5.9
$B_{eq}(nT)$:	25	70	400	2000
$\alpha_{lc}(^\circ)$:	0.34	0.56	1.37	3.14
$H^+T_{sd}(\text{days})$:	197	57	5.7	0.67
$OST_{sd}(\text{days})$:	788	226	23	2.7

The “days” are Earth days, and the loss times scale according to the square root of the energy. For example, 300 keV H^+ and OS ions would have e-folding loss times that are a factor of 1.73 shorter than those given above.

The strong diffusion e-folding times are relevant in the trans-Ganymede and near Ganymede regions, and sometimes in the regions extending halfway toward Europa. These times range from 10's of days to major fractions of an Earth year and are therefore reasonable from the perspective of energetic particle radial transport times (e.g., Krupp et al., 2004; a comparison is examined in detail for higher energy particles by Gehrels & Stone, 1983). Specifically, particle losses due to the scattering are competing with the particle transport and acceleration processes in establishing the particle populations within these regions. The processes documented in Krupp et al. (2004) are easily able to compete with the loss times documented here within the near-Ganymede and trans-Ganymede regions.

For regions where scattering falls far below the strong diffusion limit, our approach is to estimate the fraction of the strong diffusion limit that prevails within any pitch angle distribution. We examine the content of both the upgoing and downgoing loss cones using the following expression:

$$C = \sum_i \frac{\{\Omega_i \cdot [I(LCB) - I(\alpha_i)]\}}{I(LCB)} \quad (2)$$

Here, the sum is over the pitch angle bins that reside within either the upgoing or downgoing loss cone, Ω_i is the solid angle represented by pitch angle bin “i,” $I[LCB]$ is the intensity near the edge of the loss cone (the intensity for the pitch angle bin closest to $LC + \sim 8^\circ$, given the finite angle-width of JEDI where LC is the calculated loss cone), and $I[\alpha_i]$ is the intensity for pitch angle sample “i” within the respective loss cone. The solid angle associated with each pitch angle bin is $2\pi \cdot \int \sin[\alpha] d\alpha$, where the integral is over the lower and upper pitch angle bounds (e.g., $0^\circ - 9^\circ$ for the lowest bin). The ratio C_{down}/C_{up} then gives us the fraction of the loss cone that is scattered from the trapped edge of the loss cone into the loss cone. However, that is not yet the fraction of the strong diffusion limit. That ratio needs to be renormalized to the intensity values close to the magnetic equator, values that are not available to JEDI. What is available to JEDI is a lower limit to the equatorial intensities, and that is the intensity in our pitch angle plots near 90° . And so, our final “upper limit” for the fraction of the strong diffusion scattering limit is: Fraction = $(I[LCB]/I[90^\circ]) \cdot (C_{down}/C_{up})$, where the intensities are the averages of upgoing and downgoing distributions.

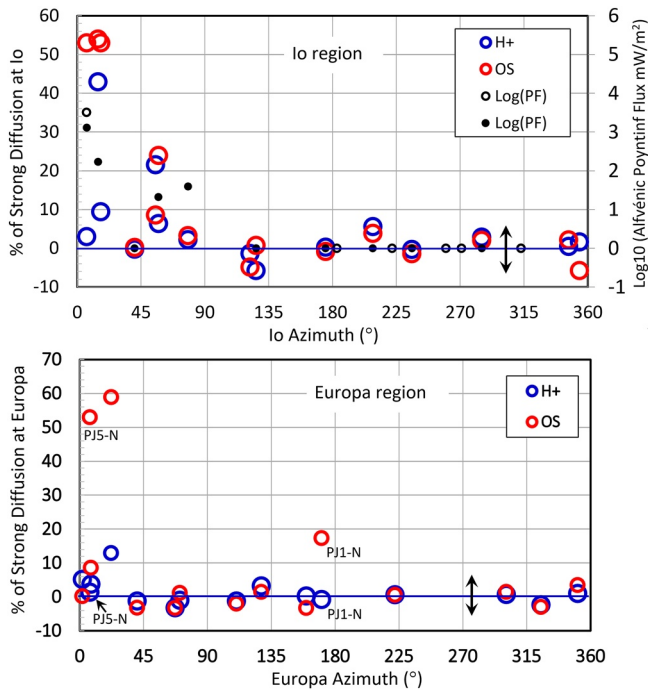


Figure 8. Results of an examination of the fill factors of the downward and upward loss cones of the pitch angle distributions measured at low altitudes by Juno for the Io regions (top panel) and the Europa regions (bottom panel). The results are expressed as a percent of the fill factor that would prevail if the ions were scattered at the strong diffusion limit. Red circles are for heavy ion distributions (OS) and blue circles are for H⁺. The x axis is the azimuth position of Io (top) and Europa (bottom) relative to the Juno sampling positions. The small black dots in the top plot (open and closed) show where Gershman et al. (2019) measured magnetic turbulence during the same or similar Juno orbits, and the Alfvénic Poynting Flux assigned to those observations. Closed dots correspond to measurements performed on the same Io orbit crossings where JEDI analysis was performed. Open dots correspond to Io orbit crossing where JEDI analysis has not been performed. The Gershman et al. (2019) observations that show no Alfvénic turbulence above the noise have been arbitrarily positioned on the “zero-line” just for display purposes.

For Io regions (on which we now focus), it is worth noting that this “upper limit” may be a closer estimate to the actual value than is obvious. When measuring equatorial pitch angle distributions, the functional form $\text{Sin}^n(\alpha)$ is often used. The published pitch angle distributions for energetic ions in the Io regions are sparse. For a 0.5–1 MeV sulfur channel at 6.6 RJ, Mauk et al. (1998; their Figure 5) suggest that an “n” value of 0.3 might be appropriate at least for the wings of the distribution, which is peaked away from 90°. For an 80–220 keV H⁺ channel at 6.7 RJ in Mauk et al. (2004; their Figure 6), one may estimate that an “n” value between 0.3 and 0.4 might be appropriate. For this discussion, we adopt here an “n” value of 0.3. To renormalize our loss cone ratio, it might be appropriate to use the equatorial pitch angle value of 60° rather than 90° since at the equator, half of the solid angle resides at pitch angle less than 60° and half resides at pitch angles greater than 60°. If we renormalize using $\text{Sin}^{0.3}[\text{ELC}]/\text{Sin}^{0.3}[60^\circ]$, (where ELC is the equatorial loss cone), we would find that our “upper limit” described above would only be lowered about 20%–25%.

Using the above-described procedure, the top panel of Figure 8 shows (with red and blue circles) a plot of the fraction (in %) of the strong diffusion limit for the Io regions as a function of the downstream azimuth position of Io relative to the observation point. The double arrow shows our estimate of the errors associated with this procedure for values that are close to zero. All of the variations for azimuth values greater than 60° are within that error estimate. Those values are all consistent with “zero” but average out to a positive fraction of 1%. It is absolutely clear that scattering is enhanced in the downstream region close to Io, but no enhancement at all appears in the upstream regions very close to Io.

We have performed various exercises in coming up with an azimuth-averaged loss fraction. For example, azimuth-average = $(60/320) \times (\text{average of points less than } 60^\circ) + (300/360) \times (\text{average of points greater than } 60^\circ)$. We arrive at about 5% for H⁺ and 7% for OS. If we use our $\text{Sin}^{0.3}[\alpha]$ to rescale rather than our local (low altitude) 90° value, we arrive at about 4% for H⁺ and 5% for OS. It is important to note that the region where these loss times apply can be very narrow as is evident in Figure 3. To apply these loss fractions to ion populations that are diffusing inward toward Io’s orbital region, we assume that the ions reside within that narrow scattering region for a substantial fraction of the population’s lifetime. Another complexity in applying these loss fractions to particle populations that are diffusing inward is the fact that in

some instances, the particle intensities are enhanced in the scattering zone, not just lost. That characteristic is shown in Figure 3 (the higher intensities associated with Io, even at 90° pitch angles), but not, for example, in Figure A3-A (where the intensities for trapped pitch angles show no enhancement over the surrounding regions). Energization is sometimes going on in addition to scattering. Do the regions just downstream of Io’s position act as a net loss to particle diffusing inward or a source of energetic ions in the energy range that is of interest here? For the present discussion, we ignore these complexities and return to them in the discussion section.

Assuming that this loss fraction applies to all of the energies measured by JEDI, the blue and left portions of Figure 9 show the e-folding loss times for the Io regions as a function of energy (scaling only according to the square root of energy as dictated by Equation 1). We find, for example, that for 200 keV H⁺, e-folding loss times are of order 10–13 days, and for 200 keV OS the loss times are of order 27–37 days.

For completeness, the bottom panel of Figure 8 shows the same analysis for the Europa regions as we performed for the Io regions. Where a specific feature was identified as associated with Europa, even when displaced from the predicted Europa location (e.g., Figure 3), we used that feature for the analysis. There are couple of lessons coming out of this analysis. In Figure 3, we noted previously the very prominent scattering feature at the near-Europa location. And at that location, the OS scattering is a major fraction of the strong diffusion limit (see the

Io Region	Strong Diffusion Days	Scat. e-fold. Loss Times (Days)		Charge Exchange cross Sections (cm ²)			CC e-folding times (Days)	
		Low	High	H+ on O	H+ on O+	Joint	Neutrals	Joint
H+(keV)	Days							
50	0.96	19.6	25.2	2.00E-16	1.50E-17	1.82E-17	5.3	1.0
80	0.76	15.5	19.9	1.30E-16	6.00E-18	8.13E-18	6.4	1.8
100	0.68	13.8	17.8	1.00E-16	4.62E-18	6.26E-18	7.5	2.1
200	0.48	9.8	12.6	1.82E-17	8.40E-19	1.14E-18	29.0	8.0
250	0.43	8.7	11.3	1.17E-17	5.40E-19	7.32E-19	40.4	11.1
300	0.39	8.0	10.3	5.20E-18	2.40E-19	7.51E-20	82.9	22.8
1000	0.21	4.4	5.6	2.50E-20	1.15E-21	1.56E-21	9448.2	2598
OS(keV)				O+ on O				
50	3.83	54.0	73.7	9.10E-16			4.6	
100	2.71	38.2	52.1	8.20E-16			4.1	
200	1.92	27.0	36.9	7.80E-16			3.8	
250	1.71	24.1	33.0	6.20E-16			3.4	
300	1.56	22.0	30.1	5.60E-16			3.4	
500	1.21	17.1	23.3	5.00E-16			3.5	
1000	0.86	12.1	16.5	2.00E-16			4.7	
2000	0.61	8.5	11.7	8.94E-17			7.5	

Figure 9. Calculated e-folding loss times in Earth days for the Io regions for scattering into the loss cones (blue regions) and for charge exchange losses (green regions). The top portion is for H⁺ and the bottom portion is for heavy ions (OS). The first green column shows ion (H⁺ or O⁺) on neutral gas (O) charge exchange cross sections as compiled from Smith et al. (2019), McEntire and Mitchell (1989), Lindsay and Stebbing (2005), and Thompson et al. (1996). The second green column shows in black, ion (H⁺) on ion (O⁺) charge exchange cross sections as estimated by Smith et al. (2019). The red numbers are very rough estimates based on the ratio between the first and second green columns at lower energies. The third green column shows weighted average cross sections using the charge and neutral density estimates for the region (2,000/cc and 35/cc, respectively; Bagenal & Dols, 2020; Brown, 1981; Skinner & Durrance, 1986) to be applied to the combined density. The last two green columns show the charge-exchange e-folding loss times based, respectively, on neutrals only and then on neutrals plus charged cross-section targets.

“PJ5-N labels in Figure 8, bottom). However, even though the H⁺ scattering is very prominent in Figure 3, the fraction of that scattering as compared to the strong diffusion limit is within the noise of the analysis. In the bottom panel of Figure 8, there is one feature that is anomalous, the relatively high scattering of OS for PJ1-N (as labeled in the Figure). It appears (see Figure A2-A) that the scattering nominally attributed to the near-Ganymede and trans-Ganymede regions has, for this particular period, extended to much lower L-shells than is typical. However, there does seem to be a modest additional enhancement just at Europa for OS. We have no explanation for that feature.

4.3. How Do Charge Exchange Losses Compare With Scattering Losses Near Io?

We here compare the derived scattering losses in Figure 9, left, with losses associated with charge exchange. We look initially just to equatorially mirroring particles that are bathed in a population of cold neutral gas and cold ions comprising the Io torus. A population $N[E]$ of energetic particles at energy E will see a change ($dN[E]$) according to the formula $dN[E] = N[E] \cdot \sigma \cdot n \cdot dx$, where σ is the charge exchange cross section with whatever low-energy population that is relevant, “ n ” is the density of that low energy population, and dx is the distance traveled by the energetic ion. Replacing dx with $V \cdot dt$ and then integrating, one obtains an exponential decrease in $N[E]$ over time with an e-folding time scale of $n\sigma V$.

The charge exchange process between energetic ions and cold neutral gas is well studied. The first green column of Figure 9 shows charge exchange cross sections between H⁺ and cold neutral oxygen and between energetic oxygen ions and cold neutral oxygen (see Figure 9 caption for literature sources). Using neutral oxygen equatorial densities of 35/cc (Brown, 1981; Lagg et al., 1998; Skinner & Durrance, 1986), one obtains the e-folding loss

times shown in the penultimate column of Figure 9. We note that uncertainty remains in the estimates of the neutral oxygen densities and their distributions around Io's orbit (Koga et al., 2018).

However, Smith et al. (2019) showed that charge exchange with charged cold oxygen ions can contribute to the charge exchange losses. For the Europa regions, the neutral gas densities are thought to be comparable to the charged ion densities, and in that case, charge exchange with neutral gas continues to dominate the charge exchange losses. However, at Io, the cold ion densities ($\sim 2,000/\text{cc}$; Bagenal & Dols, 2020) are much denser than the neutral gas densities ($\sim 35/\text{cc}$; Brown, 1981; Skinner & Durrance, 1986; obtained with optical methods). The second green column in Figure 9 shows in black letters the H^+ on O^+ charge exchange cross sections derived by Smith et al. (2019). The numbers in red are what those numbers might be at higher energies by simply applying the ratio of the H^+ on O and H^+ on O^+ cross sections shown at the low energies (50 and 80 keV) to the cross sections at higher energies. The third green column in Figure 9 shows a weighted average (weighed with density) of the charge exchange cross sections to be applied to the combined densities of cold O and O^+ . Finally, the last column of Figure 9 shows the e-folding loss times of the energetic H^+ ions using those joint, weighted cross sections. Note that there are no estimates available for O^+ on O^+ charge exchange cross sections, but that process turns out to be less important for the present discussions.

The loss times that Figure 9 provides for scattering and for charge exchange are not exactly comparable. The charge exchange loss times are estimated for equatorially mirroring particles, whereas one is interested in loss times for all pitch angles. The charge exchange loss modeling performed by Mauk et al. (1998; their Figure 5) provides an estimate of how the charge exchange losses extend to different pitch angles. For example, at 60° , the value where the solid angle contribution for different pitch angles is split exactly in two, the relative loss times are a factor of about 2.2 longer than they are for 90° particles, derived by scaling off of the “relative charge exchange survival” curve in that figure. For 45° equatorial pitch angles, the factor is about 5.6. Similarly, wave-particle interactions that lead to scattering losses often depend on a resonant condition based on the velocities of the particles along the field lines. Equatorially mirroring particles are not generally accessible to such processes. It is beyond the scope of this paper to evaluate those kinds of details in the loss processes. However, the fact that the two processes discussed here tend to act on different portions of the distributions is something that needs to be kept in mind.

A principal conclusion from Figure 9 is that charge exchange appears to completely dominate the loss of energetic ring current heavy ions (OS), irrespective of the cautions given in the previous paragraph. Sulfur ions also provide the major contribution to the particle pressures at Io and elsewhere (Mauk et al., 2004) and so the charge exchange is a critical factor in controlling the energetic particle contributions to the electric currents that comprise the ring current. The conclusions for protons (H^+) are different. At 100 keV and below, charge exchange likely dominates the loss processes. At 300 keV and above, scattering losses likely dominates the loss processes. These results were qualitatively anticipated by Paranicas et al. (2019). Between 100 and 300 keV (with a break point perhaps at 200 keV), the issues discussed in the previous paragraph become paramount with both mechanisms likely making major contributions.

5. Discussion

5.1. Wave Scattering Near Io

At the equator, Galileo observed intense EMIC waves with frequencies most often at the lowest heavy-ion gyrofrequencies (SO_2^+ and SO^+ ; e.g., Russell et al., 2001, 2003). These waves were found to be prevalent as far downstream of Io as the Galileo spacecraft sampled, specifically to a distance from Io of 10 Io radii. However, the waves were not observed in the upstream direction. The distance of 10 Io radii corresponds to a downstream azimuthal angle of 2.4° . Available Galileo data do not enable one to determine whether the EMIC waves extend further downstream from the moon as would be needed to match the Juno observation of ion scattering 60° downstream of Io. However, Wang et al. (2001) explain the observations of the Galileo EMIC waves with a model of near-Io neutral pickup, and subsequent reneutralization, that can generate more distant upstream-downstream asymmetries in these heavy ions neutrals. Saur et al. (2002) and Dols et al. (2012) also discuss upstream/downstream asymmetries in Io's atmosphere; such asymmetries could lead to asymmetries in EMIC wave generation. The observed existence of the equatorial EMIC waves downstream of Io, but not upstream of it, bears similarity

with the high-latitude azimuthal organization of ion scattering observed by JEDI. Therefore, the equatorial EMIC waves observed by Galileo represent one possible agent for the ion scattering.

However, it is also of substantial interest that Gershman et al. (2019) observed broadband Alfvénic waves in Juno magnetic field data associated with some encounters of Juno trajectories that magnetically mapped to Io's orbital position. The orbits where these waves were observed above noise levels were where Io was fairly close to, and upstream of, the measurement position. In Figure 8, we indicate with closed and open small black dots those azimuth positions and the Poynting Flux values for those observations as reported by Gershman et al. (2019). The solid dots are observations taken at essentially the same times as were the JEDI data used for the scattering analyses. The open dots are Gershman et al. (2019) observations where JEDI analysis was not performed. For those observations where wave power was at noise levels, we arbitrarily placed them on the "zero-line" for plotting convenience, just to indicate the positions of those observations.

Clearly, there is some concurrence between the observation of Alfvénic wave distributions by Gershman et al. (2019) and the JEDI observation of relatively efficient scattering of energetic ions into the loss cone. Classical Alfvén waves (non-kinetic) are not known to efficiently scatter ions. EMIC waves, known to scatter ions, have been observed at high latitude in close association with Alfvén waves in one very close encounter with Io's flux tube (Sulaiman et al., 2020). Such high-latitude EMIC waves are not obviously related to the equatorially confined EMIC waves observed by Galileo, given that their frequencies are orders of magnitude different (waves identified as EMIC scale with magnetic field strength). It may be of interest that the frequencies of the more discrete EMIC emissions at the equator are in the same range as the frequencies of the high-latitude, broadband Alfvén waves. The concurrence between the scattering and the high-latitude Alfvén waves in Figure 8 is not exact. Assuming that either these waves or waves closely associated with them are somehow involved with the scattering of the ions, we still would not know whether the scattering occurs in the vicinity of the high-latitude position of Juno or closer to the magnetic equator. The waves responsible for the scattering remain an open question.

5.2. Charge Exchange Losses

It should be no surprise that charge exchange is important for the losses for heavy ions near Io. The characteristic feature of charge exchange losses, a deep minimum in the vicinity of 90° , is very apparent in pitch angle distributions of ~ 0.5 – ~ 1.0 MeV oxygen and sulfur ions near Io's orbit (Lagg et al., 1998; Mauk et al., 1998; Williams et al., 1996).

For H^+ , the published record on pitch angle distributions is sparse. The published measurement closest to Io's orbit is that in Mauk et al. (2004) at a radial position of 6.7 RJ; 0.8 RJ outside of Io's orbit. That distribution, made with a broad energy channel ranging from 80 to 220 keV, has the classic "trapped" shape with no minimum at 90° . However, the radial series displayed in that paper (Figure 9 there) shows something very interesting. It shows the classic charge-exchange-sculpted minimum outside of 7.4 RJ, but at 7.4 RJ, the plot catches in-the-act an apparent local acceleration process filling in the strong minimum at 90° . At 7.0 RJ, that acceleration signature is all that is left. This observation reminds us that while wave-particle interactions can certainly scatter particles into the loss cone, they can also act as a source of energetic particles by energizing particles into that range from lower energies. EMIC waves can perform such a function (e.g., Nénon et al., 2018). However, the presence of such waves inside of Ulysses spacecraft minimum-L position of 8.5 RJ, where EMIC waves were observed (Lin et al., 1993), has not been documented. Such acceleration processes very near Io's flux tube at high latitude were documented by Clark, Mauk, Kollmann, Szalay, et al. (2020).

To date, the in situ tests for our conclusions about H^+ ion losses are unclear. Galileo data may have more to offer, but the clean proton measurements are broad, with the lowest energy channel covering 80–220 keV, partially overlapping our suggested transition energies. As a result of its orbit evolutions, Juno will be in the position to make definitive measurements during later orbits; perhaps PJ46 in late 2022, PJ50 in early mid 2023, and PJ58 in early 2024, based on orbit predictions regarding encounters with Io's equatorial orbit (see Acknowledgments section for sources).

There are other data that can serve to test our conclusions regarding the loss of H^+ in Io's orbit. Energetic neutral atoms (ENAs) have been observed directly coming from Io's orbit (Mauk, Clark, Allegrini, et al., 2020). These observations can be used to test the loss of H^+ ions from that region. The following calculations are used only

to demonstrate the potential of the ENA observations. There still exist substantial uncertainties. The H-ENA observations for Juno's perijove 22 (PJ22) are in Figure 4 of that paper. Counts for that observation are shown in panel (c); the densest central horizontal stripe is from Io. By assuming that the emitting region is a torus with a cross-section diameter of 2 RJ, and by considering the geometry of the observation, the sensor geometric factor, and viewing geometry of JEDI, we arrive at an emission rate for the entire torus of about 3×10^{24} H atoms/s. Note that the size of the emitting region is larger than the JEDI resolution element, and so one can begin by calculating an intensity and converting it to a flux using the solid angle of the emitting region. JEDI observes only one small slice of the of Io torus regions, and by assuming that each slice radiates uniformly into 4π steradians, and that all slices around the torus radiate the same amount, we arrive at our final estimate. The 4π steradian emission pattern is reasonable, given the flatness of the pitch angle distributions as previously discusses (e.g., $I \sim \sin^{0.3}(\alpha)$).

Several hours prior to this ENA observation, JEDI passed through the Io orbital regions (see Figure 9 in the same paper) at a magnetic latitude of about 20° – 30° , albeit at a different longitude than where the ENAs were remotely observed. Because of the flatness of the pitch angle distributions, it is expected that intensities of energetic ions will be very similar to the equatorial values. By calculating the partial density of energetic H^+ one obtains 0.015/cc for 50–130 keV, the range of energies where most of the H-ENAs reside (Panel (d) in Figure 4 of that paper). One derives a total energetic H^+ population within the emitting torus of about 4×10^{29} H^+ ions. The ratio $(4 \times 10^{29})/(3 \times 10^{24})$ is the e-folding time in our exponential expression and yields an estimate for the e-folding loss rate of about 1.5 days. However, the ENAs were observed only with one cut through the Io orbit regions, and not with the cut that occurred $\sim 180^\circ$ away. If 50% of the Io orbit regions were emitting, then the estimate would double to 3 days. These numbers, by the way, scale inversely and linearly with the assumed diameter of the emitting torus, given the two competing effects of torus content and solid angle viewing. For example, a 1 RJ diameter torus would cut the estimated e-folding times in half. While there is very substantial uncertainty in these numbers, they compare favorably with the lower energy numbers in the right-hand column in Figure 9 for H^+ .

The above-derived loss times estimated using Juno ENA observations are presented only to emphasize the potential of the ENA observations in testing the importance of charge exchange in the losses of H^+ in Io's orbit. The numbers obtained are consistent with our findings derived in Figure 9. But, more ENA observations by Juno (and future missions) must be analyzed to solidify these estimates.

5.3. Role of Scattering for the Higher Energy Protons

We note that previous analyses regarding the role of wave-particle scattering losses on energetic ions focused on MeV-class protons (Nénon et al., 2018). Our findings support the role of wave-particle losses for these very energetic H^+ . However, the character of those losses, occurring as they do primarily close to, and downstream of, Io's position can now be taken specifically into account in subsequent modeling. We reiterate that the scattering loss times in Figure 9 assume that the fractional scattering relative to the strong diffusion limit applies equally to all energies. While we do not observe energy dependence in the scattering, the statistical errors associated with that finding are relatively large.

6. Conclusions

We find in this paper that for a region mapping from just inside Ganymede's orbit to regions well beyond Ganymede's orbit, energetic ions (>50 keV H^+ and >130 keV Oxygen and Sulfur ions) are strongly scattered into the loss cone at the "strong diffusion limit" at essentially all times. Because scattering within the narrow magnetic geometries of Jupiter's neutral sheet does not appear to explain the scattering for H^+ , we conclude by elimination that waves are responsible for the scattering, perhaps associated with the Alfvénic magnetic variations previously documented by Saur et al., 2003. However, much work remains to demonstrate that the observed wave distributions (both published and that which remains to be characterized) can indeed cause the needed scattering. We note that because loss cones are so small in these regions, the loss rates associated with strong diffusion scattering do not pose a challenge to the radial transport rates that are thought to prevail at all pitch angles in these regions (e.g., Gehrels & Stone, 1983; Krupp et al., 2004).

We show that scattering into the loss cone is qualitatively weak or nonexistent near the orbits of the moons Europa and Io, except for the regions just downstream of the corotating plasmas (with one notable exception for Europa). For Io, we observe moderate, but not saturated, scattering within roughly 60° downstream. Significantly, scattering is weak or nonexistent just upstream of Io's position. There are EMIC and Alfvén wave observations with upstream-downstream asymmetries that might have a role in the asymmetric scattering, but at this point in time it is unresolved what waves are responsible.

A preliminary accounting of the total scattering losses near Io's orbit yields loss rates of order 4%–5% of the strong diffusion limit for H^+ , and 5%–7% for heavy ions (O + S). We conclude that near Io's orbit, charge exchange losses are likely dominant over scattering losses for heavy ions (providing the major contribution to the particle pressures) and for the lower energy H^+ (perhaps roughly <200 keV).

Our conclusions about charge exchange losses for heavy ions (OS) are supported by previous observations of equatorial pitch angle distributions. These distributions show the characteristic minimum near 90° pitch angles. In situ tests of our conclusions about H^+ ions await future orbits of the Juno mission. However, our conclusions about charge exchange losses for the lower energy H^+ are supported, although not proven, by the earlier reported ENA observations from the vicinity of Io's orbit.

Appendix A

Placed here are additional examples of the perijove passes where scattering analyses have been performed. These additional examples include (a) perijoves where the moons Io and Europa are a long way in azimuth from the Juno observations position (Figures A1-A, A1-B, A2-A, and A2-B), (b) perijoves where Io, and sometimes Europa, are nearby and upstream (Figures A3-A, A3-B, A4-A, and A4-B), and (c) a figure where Io is nearby and downstream (Figure A5).

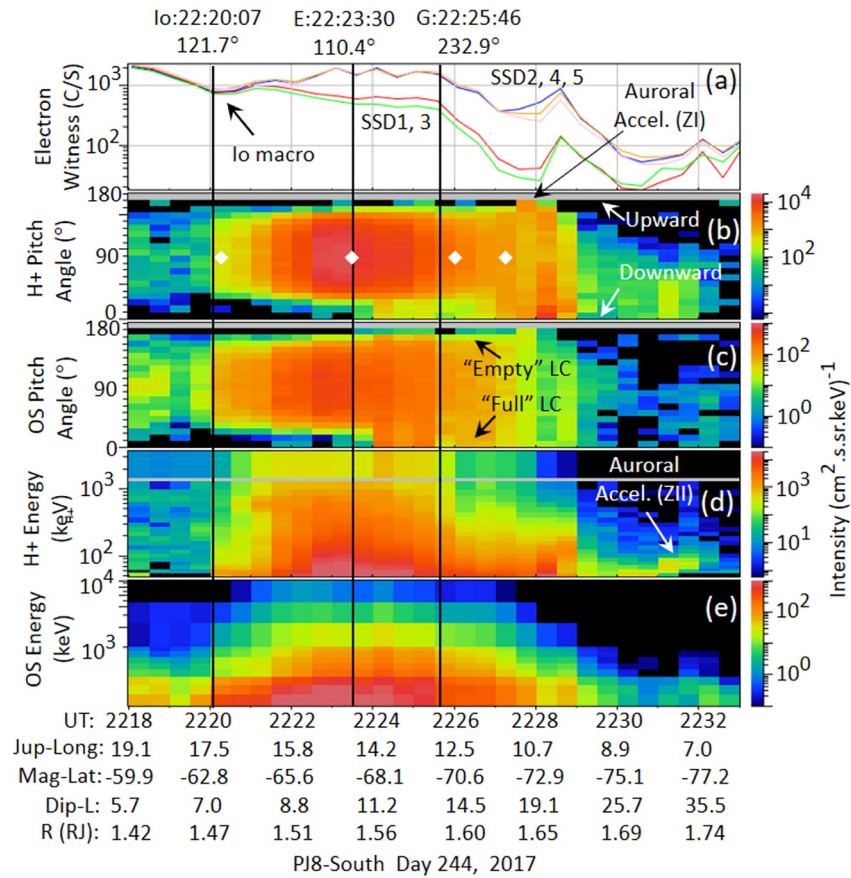


Figure A1-A. Same as Figure 1 except that it is for the time period of the Juno southern perijove 8 (PJ8-S). For this period of time, Io and Europa are far away in azimuth from the Juno satellite crossing positions.

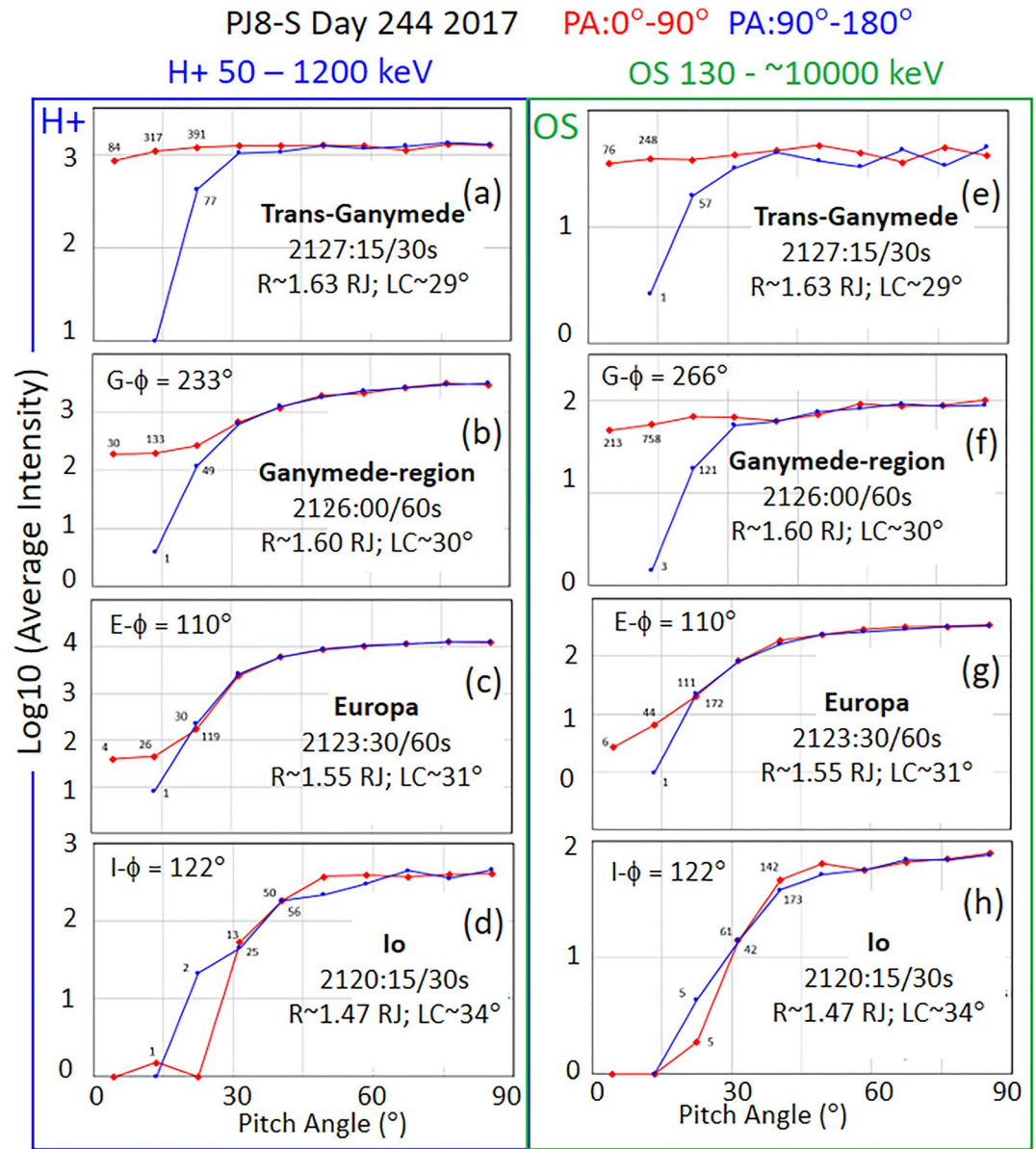


Figure A1-B. Same as Figure 2 except that it refers to the time period of Figure A1-A.

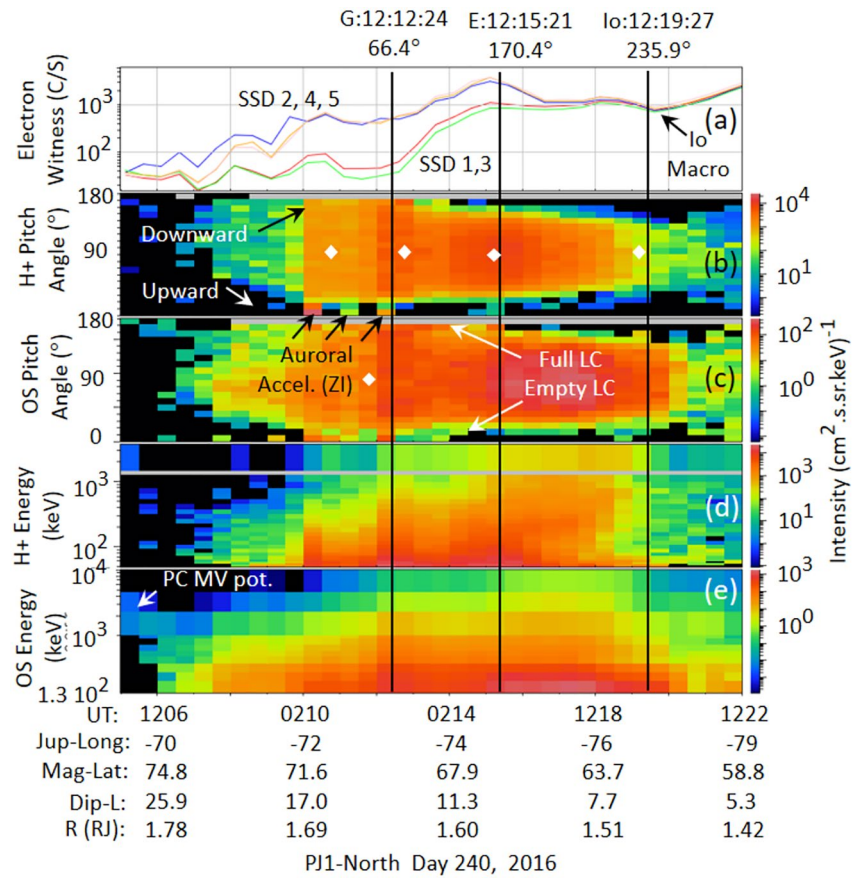


Figure A2-A. Same as Figure 1 except that it is for the time period of the Juno northern perijove 1 (PJ1-N). For this period of time, Io and Europa are far away in azimuth from the Juno satellite-crossing positions.

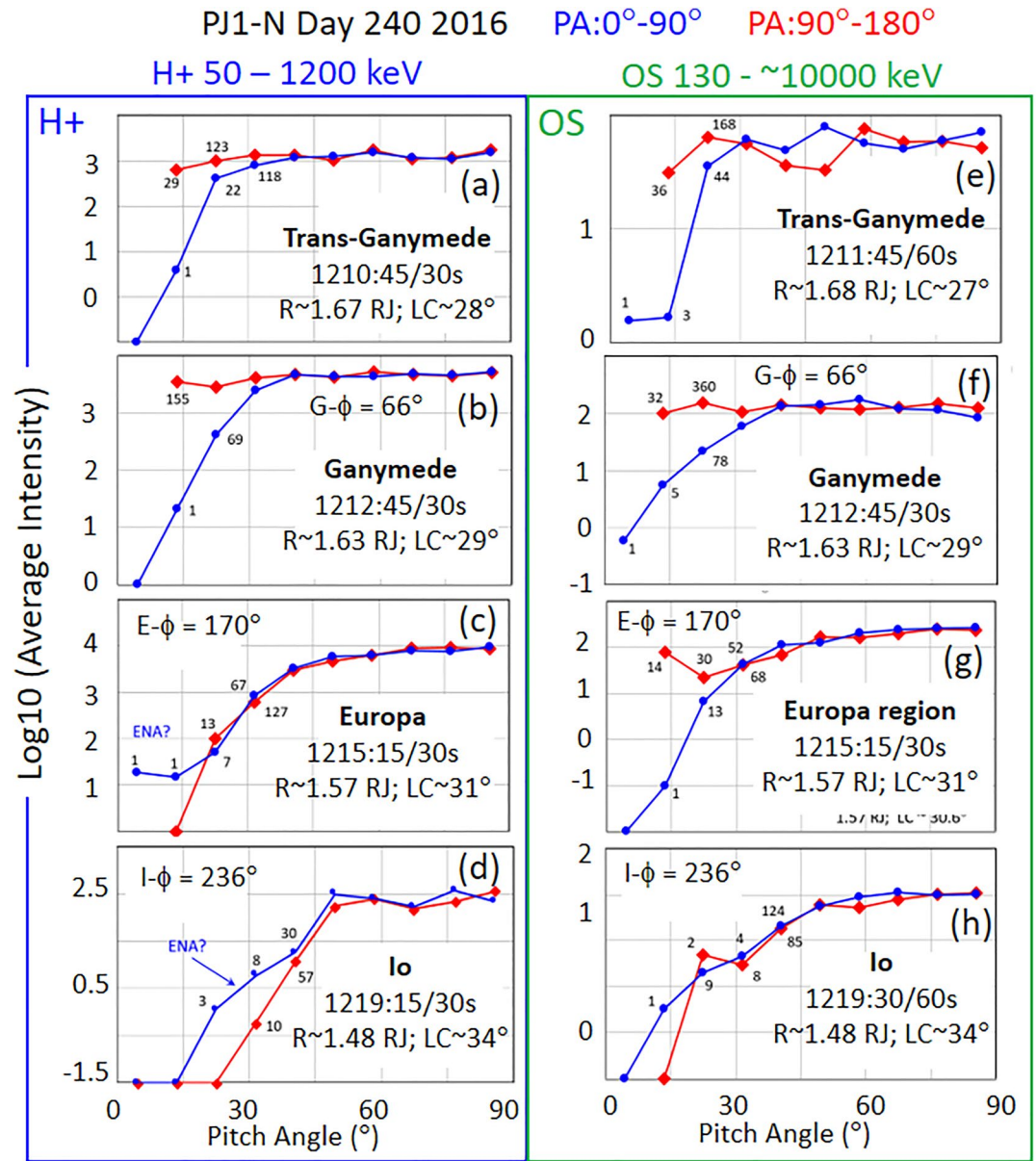


Figure A2-B. Same as Figure 2 except that it refers to the time period of Figure A2-A.

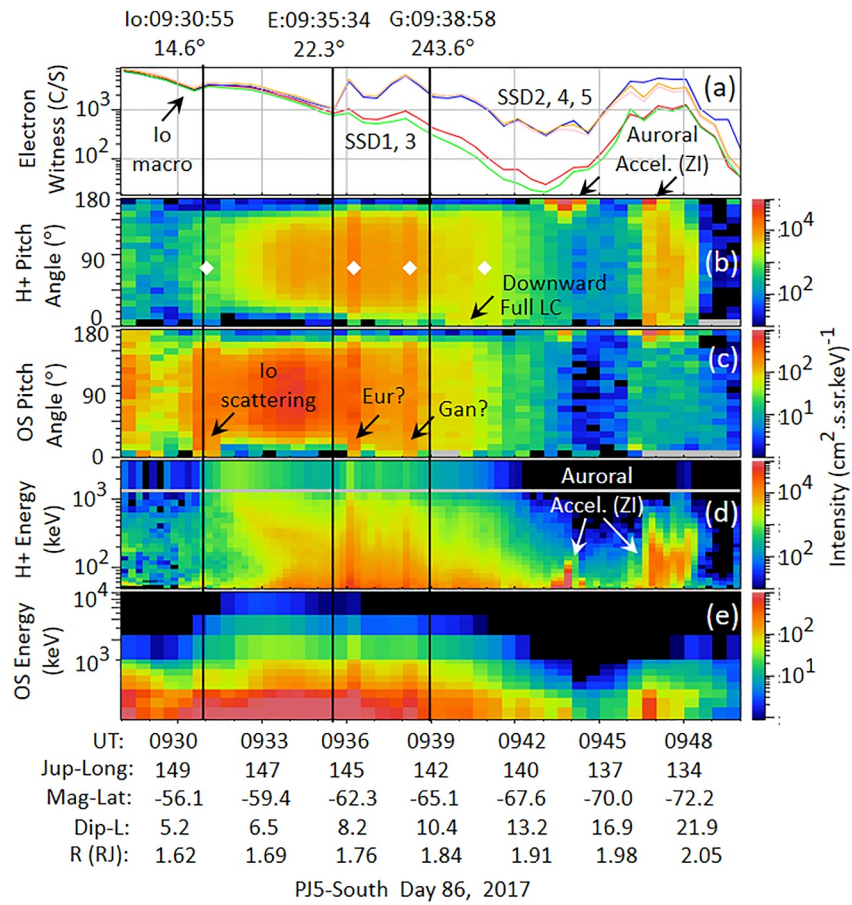


Figure A3-A. Same as Figure 1 except that it is for the time period of the Juno southern perijove 5 (PJ5-S). For this period of time, Io and Europa are close in azimuth in the upstream direction from the Juno satellite-crossing positions.

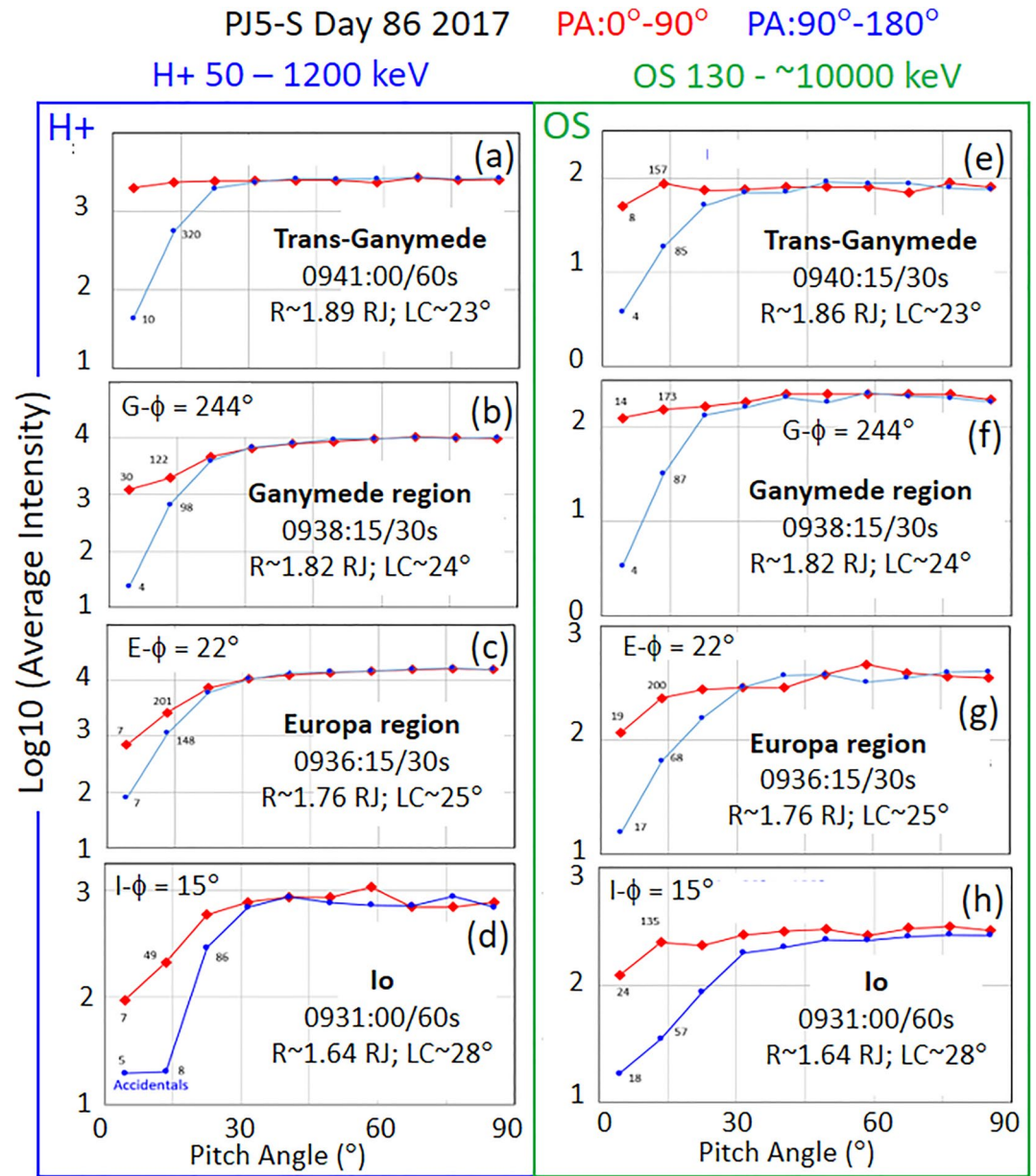


Figure A3-B. Same as Figure 2 except that it refers to the time period of Figure A3-A.

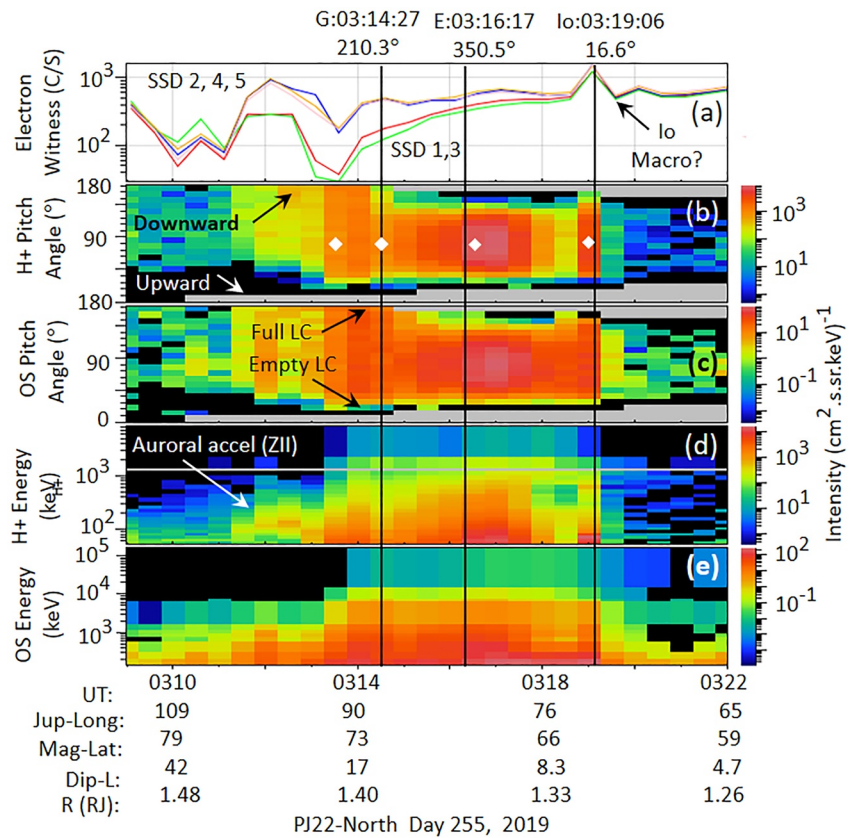


Figure A4-A. Same as Figure 1 except that it is for the time period of the Juno northern perijove 22 (PJ22-N). For this period of time, Io is close and upstream in azimuth, and Europa is close and downstream in azimuth, from the Juno satellite-crossing positions.

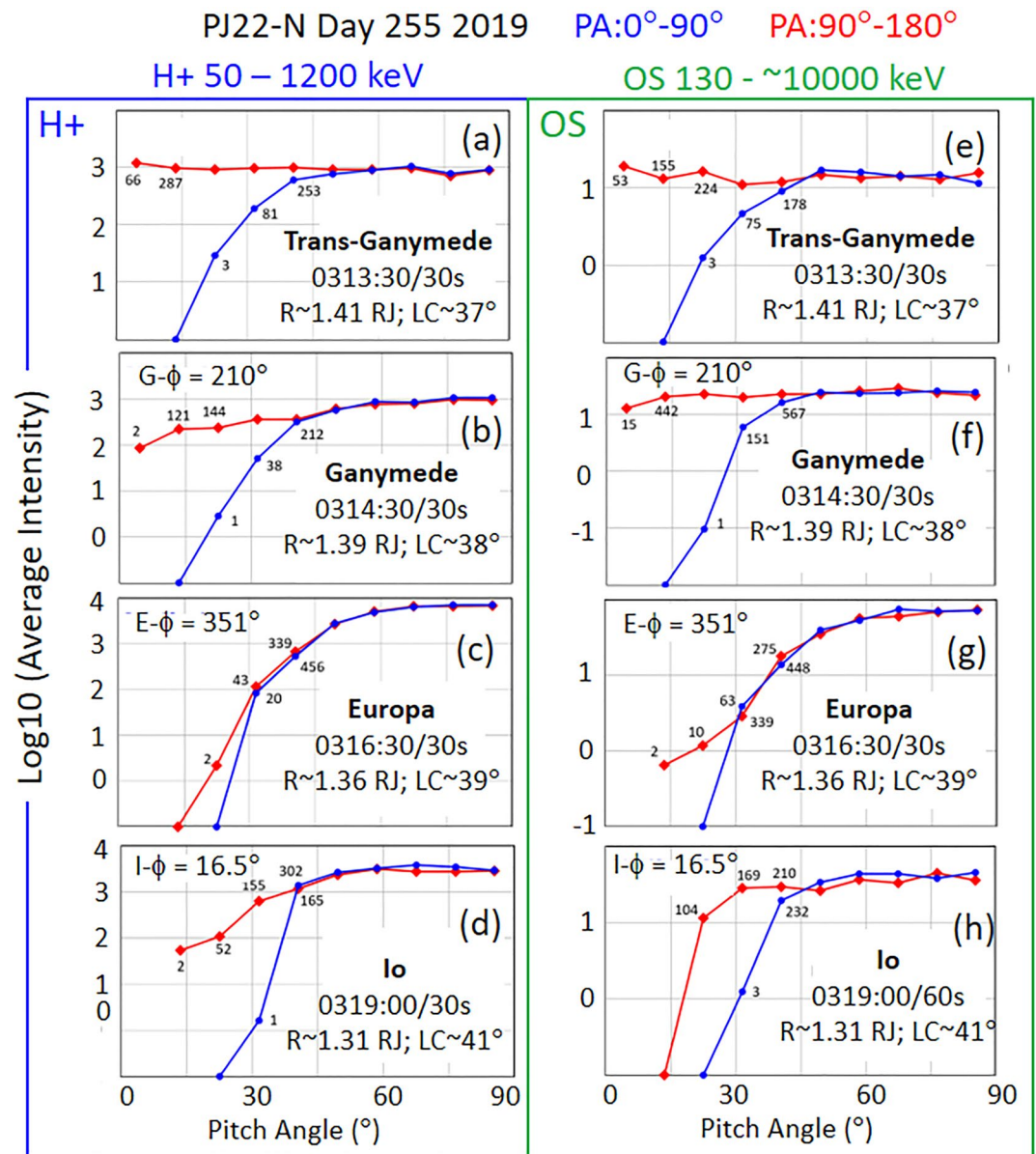


Figure A4-B. Same as Figure 2 except that it refers to the time period of Figure A4-A.

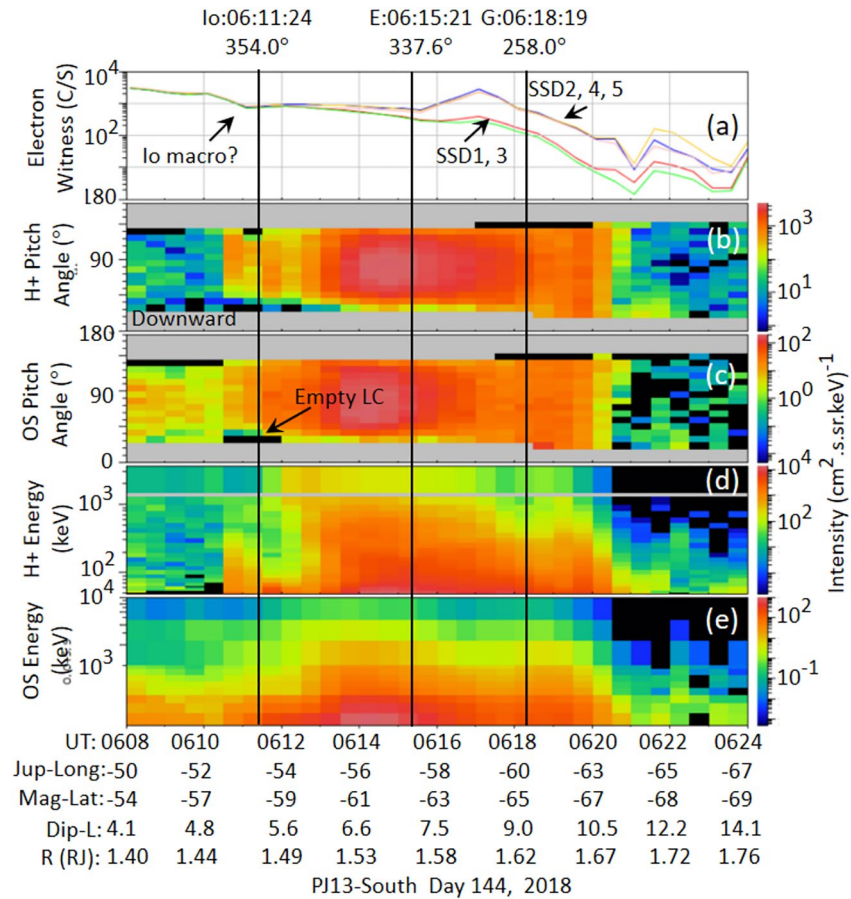


Figure A5. Same as Figure 1 except that it is for the time period of the Juno southern perijove 13 (PJ13-S). For this period of time, Io is close in azimuth in the downstream direction from the Juno satellite-crossing position.

Data Availability Statement

The data presented here are available from the Planetary Plasma Interactions Node of NASA's Planetary Data System (<https://pds-ppi.igpp.ucla.edu/>). Also, ASCII dumps with header documentation have been performed for each panel of the JEDI data displayed in this paper and are accessible at zenodo (doi:10.5281/zenodo.6380871). The JEDI display software used here is available online and can be accessed by contacting the lead author. A 1-hr teleconference tutorial provided by the lead author or his designate is generally sufficient for a user to have sufficient expertise to proceed. Information about the predicted future orbits of Juno, and information about the calculations and the results of Juno crossings of the plasma tails of the moons Ganymede, Europa, and Io of Juno, can be found at <https://lasp.colorado.edu/home/mop/missions/juno/trajectory-information/>.

References

- Allegri, F., Bagenal, F., Bolton, S., Connerney, J., Clark, G., Ebert, R. W., et al. (2017). Electron beams and loss cones in the auroral regions of Jupiter. *Geophysical Research Letters*, 44(14), 7131–7139. <https://doi.org/10.1002/2017GL073180>
- Allegri, F., Gladstone, G. R., Hue, V., Clark, G., Szalay, J. R., Kurth, W. S., et al. (2020). First report of electron measurements during a Europa footprint tail crossing by Juno. *Geophysical Research Letters*, 47, e2020GL089732. <https://doi.org/10.1029/2020GL089732>
- Allegri, F., Mauk, B., Clark, G., Gladstone, G. R., Hue, V., Kurth, W. S., et al. (2020). Energy flux and characteristic energy of electrons over Jupiter's main auroral emission. *Journal of Geophysical Research: Space Physics*, 125, e2019JA027693. <https://doi.org/10.1029/2019JA027693>
- Bagenal, F., & Dols, V. (2020). The space environment of Io and Europa. *Journal of Geophysical Research: Space Physics*, 125(5), e2019JA027485. <https://doi.org/10.1029/2019JA027485>
- Bhattacharya, B., Thorne, R. M., & Williams, D. J. (2001). On the energy source for diffuse auroral emissivity. *Geophysical Research Letters*, 28(14), 2751–2754. <https://doi.org/10.1029/2000GL012616>
- Birmingham, T. J. (1982). Charged particle motions in the distended magnetospheres of Jupiter and Saturn. *Journal of Geophysical Research*, 87(A9), 7421–7430. <https://doi.org/10.1029/JA087iA09p07421>

Acknowledgments

We are grateful to NASA and contributing institutions that played critical roles in making the Juno mission possible, and particularly those numerous individuals at The Johns Hopkins University Applied Physics Laboratory (JHU/APL) who developed the JEDI instrument. We are grateful for Lead Engineer Charles E Schlemm and David B. LaVallee for their continued support of JEDI operations. We are grateful to JHU/APL's Lawrence E. Brown and James M. Peachey for their roles in developing and maintaining the data flow and display software used here. NASA's New Frontiers Program funded much of this work for Juno via subcontract with the Southwest Research Institute. The work of M. Imai was supported by the JSPS KAKENHI Grant No. JP20K22371. Q. Nénon acknowledges support from the European Space Agency (ESA) as an ESA Research Fellow.

- Bolton, S. J., Lunine, J., Stevenson, D., Connerney, J. E. P., Levin, S., Owen, T. C., et al. (2017). The Juno mission. *Space Science Reviews*, 213(1–4), 5–37. <https://doi.org/10.1007/s11214-017-0429-6>
- Brandt, P. C., Hsieh, S. Y., DeMajistre, R., & Mitchell, D. G. (2018). ENA imaging of planetary ring currents. In A. Keiling, O. Marghitu, & M. Wheatland (Eds.), *Electric currents in geospace and beyond. Geophysical monograph 235* (pp. 139–154). American Geophysical Union. Chapter 9. <https://doi.org/10.1002/9781119324522>
- Brown, R. A. (1981). The Jupiter hot plasma torus - Observed electron temperature and energy flows. *Astrophysical Journal*, 1(244), 1072–1080. <https://doi.org/10.1086/158777>
- Büchner, J., & Zelenyi, L. M. (1989). Regular and chaotic charged particle motion in magnetotail-like field reversals: 1. Basic theory of trapped motion. *Journal of Geophysical Research*, 94(A9), 11842. <https://doi.org/10.1029/JA094iA09p11821>
- Cao, X., Ni, B., Liang, J., Xiang, Z., Wang, Q., Shi, R., et al. (2016). Resonant scattering of central plasma sheet protons by multi-band EMIC waves and resultant proton loss timescales. *Journal of Geophysical Research: Space Physics*, 121(2), 1219–1232. <https://doi.org/10.1002/2015JA021933>
- Caudal, G. (1986). A self-consistent model of Jupiter's magnetodisc including the effects of centrifugal force and pressure. *Journal of Geophysical Research*, 91(A4), 4201–4221. <https://doi.org/10.1029/JA091iA04p04201>
- Clark, G., Mauk, B. H., Haggerty, D., Paranicas, C., Kollmann, P., Rymer, A., et al. (2017). Energetic particle signatures of magnetic field-aligned potentials over Jupiter's polar regions. *Geophysical Research Letters*, 44(17), 8703–8711. <https://doi.org/10.1002/2017GL074366>
- Clark, G., Mauk, B. H., Kollmann, P., Paranicas, C., Bagenal, F., Allen, R. C., et al. (2020). Heavy ion charge states in Jupiter's polar magnetosphere inferred from auroral megavolt electric potentials. *Journal of Geophysical Research: Space Physics*, 125. e2020JA028052. <https://doi.org/10.1029/2020JA028052>
- Clark, G., Mauk, B. H., Kollmann, P., Szalay, J. R., Sulaiman, A. H., Gershman, D. J., et al. (2020). Energetic proton acceleration associated with Io's footprint tail. *Geophysical Research Letters*, 47(24), e2020GL090839. <https://doi.org/10.1029/2020GL090839>
- Clark, G., Mauk, B. H., Paranicas, C., Kollmann, P., & Smith, H. T. (2016). Charge states of energetic oxygen and sulfur ions in Jupiter's magnetosphere. *Journal of Geophysical Research: Space Physics*, 121(3), 2264–2273. <https://doi.org/10.1002/2015JA022257>
- Connerney, J. E. P., Acuña, M. H., & Ness, N. F. (1981). Modeling the Jovian current sheet and inner magnetosphere. *Journal of Geophysical Research*, 86(A10), 8370–8384. <https://doi.org/10.1029/JA086iA10p08370>
- Connerney, J. E. P., Benn, M., Bjarno, J. B., Denver, T., Espley, J., Jorgensen, J. L., et al. (2017). The Juno magnetic field investigation. *Space Science Reviews*, 213(104), 39–138. <https://doi.org/10.1007/s11214-017-0334-z>
- Connerney, J. E. P., Kotsiaros, S., Oliverson, R. J., Espley, J. R., Joergensen, J. L., Joergensen, P. S., et al. (2018). A new model of Jupiter's magnetic field from Juno's first nine orbits. *Geophysical Research Letters*, 45, 2590–2596. <https://doi.org/10.1002/2018GL077312>
- Connerney, J. E. P., Timmins, S., Herceg, M., & Joergensen, J. L. (2020). A Jovian magnetodisc model for the Juno era. *Journal of Geophysical Research: Space Physics*, 125. <https://doi.org/10.1029/2020JA028138>
- Dols, V., Delamere, P. A., Bagenal, F., Kurth, W. S., & Paterson, W. R. (2012). Asymmetry of Io's outer atmosphere: Constraints from five Galileo flybys. *Journal of Geophysical Research*, 117(E10), E10010. <https://doi.org/10.1029/2012JE004076>
- Gehrels, N., & Stone, E. C. (1983). Energetic oxygen and sulfur ions in the Jovian magnetosphere and their contribution to the auroral excitation. *Journal of Geophysical Research*, 88(A7), 5537–5550. <https://doi.org/10.1029/JA088iA07p05537>
- Gershman, D. J., Connerney, J. E. P., Kotsiaros, S., DiBraccio, G. A., Martos, Y. M., F-Viñas, A., et al. (2019). Alfvénic fluctuations associated with Jupiter's auroral emissions. *Geophysical Research Letters*, 46, 7157–7165. <https://doi.org/10.1029/2019GL082951>
- Haggerty, D. K., Mauk, B. H., Paranicas, C. P., Clark, G., Kollmann, P., Rymer, A. M., et al. (2019). Jovian injections observed at high latitude. *Geophysical Research Letters*, 46(16), 9397–9404. <https://doi.org/10.1029/2019GL083442>
- Jordanova, V. K. (2020). Ring current decay. In V. K. Jordanova, R. Ilie, & M. W. Chen (Eds.), *Ring current investigations; the quest for space weather prediction* (pp. 153–224). Elsevier. (ISBN: 978-0-12-815571-4978-0-12-815572-1).
- Kirsch, E., Krimigis, S. M., Kohl, J. W., & Keath, E. P. (1981). Upper limits for X-ray and energetic neutral particle emission from Jupiter: Voyager-1 results. *Geophysical Research Letters*, 8, 169–172. <https://doi.org/10.1029/GL008i002p00169>
- Koga, R., Tsuchiya, F., Kagitani, M., Sakanoi, T., Yoneda, M., Yoshioka, K., et al. (2018). Spatial distribution of Io's neutral oxygen cloud observed by Hisaki. *Journal of Geophysical Research: Space Physics*, 123(5), 3764–3776. <https://doi.org/10.1029/2018JA025328>
- Kollmann, P., Paranicas, C., Clark, G., Mauk, B. H., Haggerty, D. K., Rymer, A. M., et al. (2017). A heavy ion and proton radiation belt inside of Jupiter's rings. *Geophysical Research Letters*, 44(11), 5259–5268. <https://doi.org/10.1002/2017GL073730>
- Krimigis, S., Mitchell, D., Hamilton, D., Dandouras, J., Armstrong, T. P., Bolton, S. J., et al. (2002). A nebula of gases from Io surrounding Jupiter. *Nature*, 415, 994–996. <https://doi.org/10.1038/415994a>
- Krupp, N., Vasyliūnas, V. M., Wock, J., Lagg, A., Khurana, K. K., Kivelson, M. G., et al. (2004). Dynamics of the Jovian magnetosphere. In F. Bagenal, T. Dowling, & W. McKinnon (Eds.), *Satellites and magnetosphere*. Cambridge Planetary Science, Cambridge University Press.
- Lagg, A., Krupp, N., Wock, J., Livi, S., Wilken, B., & Williams, D. J. (1998). *Determination of the neutral number density in the Io Torus from Galileo-EPD measurements*. 21, 4039–4042. <https://doi.org/10.1029/1998GL900070>
- Lavraud, B., Zhang, Y. C., Vernisse, Y., Gershman, D. J., Dorelli, J., Cassak, P. A., et al. (2016). Currents and associated electron scattering and bouncing near the diffusion region at Earth's magnetopause. *Geophysical Research Letters*, 43(7), 3042–3050. <https://doi.org/10.1002/2016GL068359>
- Li, W., Ma, Q., Shen, X.-C., Zhang, X.-J., Mauk, B. H., Clark, G., et al. (2021). Quantification of diffuse auroral electron precipitation driven by whistler mode waves at Jupiter. *Geophysical Research Letters*, 48, e2021GL095457. <https://doi.org/10.1029/2021GL095457>
- Liang, J., Donovan, E., Ni, B., Yue, C., Jiang, F., & Angelopoulos, V. (2014). On an energy-latitude dispersion pattern of ion precipitation potentially associated with magnetospheric EMIC waves. *Journal of Geophysical Research: Space Physics*, 119(10), 8137–8160. <https://doi.org/10.1002/2014JA020226>
- Lin, N., Kellogg, P. J., MacDowall, R. J., Mei, Y., Cornilleau-Wehrin, N., Canu, P., et al. (1993). ULF waves in the Io torus: Ulysses observations. *Journal of Geophysical Research*, 98(A12), 21162. <https://doi.org/10.1029/93JA02593>
- Lindsay, B. G., & Stebbing, R. F. (2005). Charge transfer cross sections for energetic neutral atom data analysis. *Journal of Geophysical Research*, 110, A12.
- Liu, Z.-Y., Zong, Q.-G., Blanc, M., Sun, Y.-X., Zhao, J.-T., Hao, Y.-X., & Mauk, B. H. (2021). Statistics on Jupiter's current sheet with Juno data: Geometry, magnetic fields and energetic particles. *Journal of Geophysical Research: Space Physics*, 126(11), e2021JA029710. <https://doi.org/10.1029/2021JA029710>
- Lyons, L. R., & Williams, D. J. (1984). *Quantitative aspects of magnetospheric Physics*. Springer-Science+Business Media.
- Mauk, B. H., Allegrini, F., Bagenal, F., Bolton, S. J., Clark, G., Connerney, J. E. P., et al. (2020). Energetic neutral atoms from Jupiter's polar regions. *Journal of Geophysical Research: Space Physics*, 125, e2020JA028697. <https://doi.org/10.1029/2020JA028697>

- Mauk, B. H., Clark, G., Allegrini, F., Bagenal, F., Bolton, S. J., Connerney, J. E. P., et al. (2020). Juno energetic neutral atom (ENA) remote measurements of magnetospheric injection dynamics in Jupiter's Io torus regions. *Journal of Geophysical Research: Space Physics*, *125*, e2020JA027964. <https://doi.org/10.1029/2020JA027964>
- Mauk, B. H., Clark, G., Gladstone, G. R., Kotsiaros, S., Adriani, A., Allegrini, F., et al. (2020). Energetic particles and acceleration regions over Jupiter's polar cap and main aurora; a broad overview. *Journal of Geophysical Research: Space Physics*, *125*(3), e2019JA027699. <https://doi.org/10.1029/2019JA027699>
- Mauk, B. H., Haggerty, D. K., Jaskulek, S. E., Schlemm, C. E., Brown, L. E., Cooper, S. A., et al. (2017). The Jupiter energetic particle detector instrument (JEDI) investigation for the Juno mission. *Space Science Reviews*, *213*(1–4), 289–346. <https://doi.org/10.1007/s11214-013-0025-3>
- Mauk, B. H., Haggerty, D. K., Paranicas, C., Clark, G., Kollmann, P., Rymer, A. M., et al. (2017). Juno observations of energetic charged particles over Jupiter's polar regions: Analysis of monodirectional and bidirectional electron beams. *Geophysical Research Letters*, *44*(10), 4410–4418. <https://doi.org/10.1002/2016GL072286>
- Mauk, B. H., Keath, E. P., & Krimigis, S. M. (1994). Unusual satellite-electron signature within the Uranian magnetosphere and its implications regarding whistler electron loss processes. *Journal of Geophysical Research*, *99*(A10), 19441–19450. <https://doi.org/10.1029/94JA01658>
- Mauk, B. H., & Krimigis, S. M. (1987). Radial force balance within Jupiter's dayside magnetosphere. *Journal of Geophysical Research*, *92*(A9), 9931–9941. <https://doi.org/10.1029/JA092iA09p09931>
- Mauk, B. H., McEntire, R. W., Williams, D. J., Lagg, A., Roelof, E. C., Krimigis, S. M., et al. (1998). Galileo-measured depletion of near-Io hot ring current plasmas since the Voyager epoch. *Journal of Geophysical Research*, *103*(A3), 4715–4722. <https://doi.org/10.1029/97JA02343>
- Mauk, B. H., Mitchell, D. G., Krimigis, S. M., Roelof, E. C., & Paranicas, C. P. (2003). Energetic neutral atoms from a trans-Europa gas torus at Jupiter. *Nature*, *421*(6926), 920–922. <https://doi.org/10.1038/nature01431>
- Mauk, B. H., Mitchell, D. G., McEntire, R. W., Paranicas, C. P., Roelof, E. C., Williams, D. J., et al. (2004). Energetic ion characteristics and neutral gas interactions in Jupiter's magnetosphere. *Journal of Geophysical Research*, *109*(A9), A09S12. <https://doi.org/10.1029/2003JA010270>
- Mauk, B. H., & Saur, J. (2007). Equatorial electron beams and auroral structuring at Jupiter. *Journal of Geophysical Research*, *112*(A10), A10221. <https://doi.org/10.1029/2007JA012370>
- Mauk, B. H., Saur, J., Mitchell, D. G., Roelof, E. C., Brandt, P. C., Armstrong, T. P., et al. (2005). Energetic particle injections in Saturn's magnetosphere. *Geophysical Research Letters*, *32*(14), L14S05. <https://doi.org/10.1029/2005GL022485>
- McEntire, R. W., & Mitchell, D. G. (1989). Instrumentation for global magnetospheric imaging via energetic neutral atoms. In J. H. Waite, J. L. Burch, & R. L. Moore (Eds.), *Solar system plasma Physics*. <https://doi.org/10.1029/GM054p0069>
- McNutt, R. L., Jr. (1984). Force balance in the outer planet magnetospheres. In H. S. Bridge, J. W. Belcher, T. S. Chang, B. Coppi, & J. R. Jasperse (Eds.), *Proceedings of the 1982-4 symposia on the Physics of space plasmas*. Scientific Publishers.
- Mitchell, D. G., Paranicas, C. P., Mauk, B. H., Roelof, E. C., & Krimigis, S. M. (2004). Energetic neutral atoms from Jupiter measured with the Cassini magnetospheric imaging instrument: Time dependence and composition. *Journal of Geophysical Research*, *109*(A9), A09S11. <https://doi.org/10.1029/2003JA010120>
- Nénon, Q., & André, N. (2019). Evidence of Europa neutral gas torii from energetic sulfur ion measurements. *Geophysical Research Letters*, *46*(7), 3599–3606. <https://doi.org/10.1029/2019GL082200>
- Nénon, Q., Sicard, A., Kollmann, P., Garrett, H. B., Sauer, S. P. A., & Paranicas, C. (2018). A physical model of the proton radiation belts of Jupiter inside Europa's orbit. *Journal of Geophysical Research: Space Physics*, *123*(5), 3512–3532. <https://doi.org/10.1029/2018JA025216>
- Paranicas, C., Mauk, B. H., Haggerty, D. K., Clark, G., Kollmann, P., Rymer, A. M., et al. (2019). Io's effect on energetic charged particles as seen in Juno data. *Geophysical Research Letters*, *46*, 13615–13620. <https://doi.org/10.1029/2019GL085393>
- Paranicas, C. P., Mauk, B. H., & Krimigis, S. M. (1991). Pressure anisotropy and radial stress balance in the Jovian neutral sheet. *Journal of Geophysical Research*, *96*(A12), 21135–21140. <https://doi.org/10.1029/91JA01647>
- Pensionerov, I. A., Alexeev, I. I., Belenkaya, E. S., Connerney, J. E. P., & Cowley, S. W. H. (2019). Model of Jupiter's current sheet with a piecewise current density. *Journal of Geophysical Research: Space Physics*, *124*, 1843–1854. <https://doi.org/10.1029/2018JA026321>
- Pensionerov, I. A., Cowley, S. W. H., Belenkaya, E. S., & Alexeev, I. I. (2021). Axially asymmetric steady state model of Jupiter's magnetosphere-ionosphere coupling. *Journal of Geophysical Research: Space Physics*, *126*(11), e2021JA029608. <https://doi.org/10.1029/2021JA029608>
- Russell, C. T., Blanco-Cano, X., Wang, Y. L., & Kivelson, M. G. (2003). Ion cyclotron waves at Io: Implications for the temporal variation of io's atmosphere, planet. *Space Physics*, *51*(14–15), 14937–15015. <https://doi.org/10.1016/j.pss.2003.05.005>
- Russell, C. T., Wang, Y. L., Blanco-Cano, X., & Strangeway, R. J. (2001). The Io mass-loading disk: Constraints provided by ion cyclotron wave observations. *Journal of Geophysical Research*, *106*(A11), 26233–26242. <https://doi.org/10.1029/2001JA900029>
- Saur, J., Janser, S., Schreiner, A., Clark, G., Mauk, B. H., Kollmann, P., et al. (2018). Wave-particle interaction of Alfvén waves in Jupiter's magnetosphere: Auroral and magnetospheric particle acceleration. *Journal of Geophysical Research: Space Physics*, *123*, 9560–9573. <https://doi.org/10.1029/2018JA025948>
- Saur, J., Neubauer, F. M., Strobel, D. F., & Summers, M. E. (2002). Interpretation of Galileo's Io plasma and field observations: I0, I24, and I27 flybys and close polar passes. *Journal of Geophysical Research*, *107*(A12), 1422. <https://doi.org/10.1029/2001JA005067>
- Saur, J., Pouquet, A., & Matthaeus, W. H. (2003). An acceleration mechanism for the generation of the main auroral oval on Jupiter. *Geophysical Research Letters*, *30*, 1260. <https://doi.org/10.1029/2002GL015761>
- Selesnick, R. S., Cohen, C. M. S., & Khurana, K. K. (2001). Energetic ion dynamics in Jupiter's plasma sheet. *Journal of Geophysical Research*, *106*(A9), 18895–18905. <https://doi.org/10.1029/2000JA000242>
- Sergeev, V. A., Sazhina, E. M., Tsyganenko, N. A., Lundblad, J. Å., & Søraas, F. (1983). Pitch-angle scattering of energetic protons in the magnetotail current sheet as the dominant source of their isotropic precipitation into the nightside ionosphere. *Planetary and Space Science*, *31*(10), 1147–1155. [https://doi.org/10.1016/0032-0633\(83\)90103-4](https://doi.org/10.1016/0032-0633(83)90103-4)
- Skinner, T. E., & Durrance, S. T. (1986). Neutral oxygen and sulfur densities in the Io Torus. *The Astrophysical Journal*, *310*, 996. <https://doi.org/10.1086/164747>
- Smith, H. T., Mitchell, D. G., Johnson, R. E., Mauk, B. H., & Smith, J. E. (2019). Europa neutral torus confirmation and characterization based on observations and modeling. *The Astrophysical Journal*, *871*, 69. <https://doi.org/10.3847/1538-4357/aaed38>
- Smyth, S. H., & Marconi, M. L. (2006). Europa's atmosphere, gas tori, and magnetospheric implications. *Ecarus*, *181*(2), 510. <https://doi.org/10.1016/j.icarus.2005.10.019>
- Smyth, W. H., & Marconi, M. L. (2003). Nature of the iogenic plasma source in Jupiter's magnetosphere: I. Circumplanetary distribution. *Icarus*, *181*(Issue 2), 510–526. ISSN 0019-1035. [https://doi.org/10.1016/S0019-1035\(03\)00176-3](https://doi.org/10.1016/S0019-1035(03)00176-3)
- Sulaiman, A. H., Hospodarsky, G. B., Elliott, S. S., Kurth, W. S., Gurnett, D. A., Imai, M., et al. (2020). Wave-particle interactions associated with Io's auroral footprint: Evidence of Alfvén, ion cyclotron, and whistler modes. *Geophysical Research Letters*, *47*, e2020GL088432. <https://doi.org/10.1029/2020GL088432>

- Thompson, W. R., Shah, M. B., & Gilbody, H. B. (1996). One-electron capture in collisions of 6 - 100 keV protons with oxygen atoms. *Journal of Physics B: Atomic, Molecular and Optical Physics*, 29(4), 725–732. <https://doi.org/10.1088/0953-4075/29/4/014>
- Thomsen, M. F., Goertz, C. K., & Van Allen, J. A. (1977). On determining magnetospheric diffusion coefficients from the observed effects of Jupiter's satellite Io. *Journal of Geophysical Research*, 82(35), 5541–5550. <https://doi.org/10.1029/JA082i035p05541>
- Tomás, A. T., Woch, J., Krupp, N., Lagg, A., Glassmeier, K.-H., & Kurth, W. S. (2004). Energetic electrons in the inner part of the Jovian magnetosphere and their relation to auroral emissions. *Journal of Geophysical Research*, 109(A6), A06203. <https://doi.org/10.1029/2004JA010405>
- Wang, Y., Russell, C. T., & Raeder, J. (2001). The Io mass-loading disk: Model calculations. *Journal of Geophysical Research*, 106(A11), 26243–26260. <https://doi.org/10.1029/2001JA900062>
- Williams, D. J., Mauk, B. H., McEntire, R. E., Roelof, E. C., Armstrong, T. P., Wilken, B., et al. (1996). Electron beams and ion composition measured at Io and in its Torus. *Science*, 274, 5286–5403. <https://doi.org/10.1126/science.274.5286.401>
- Yahnin, A. G., Popova, T. A., Demekhov, A. G., Lubchich, A. A., Matsuoka, A., Asamura, K., et al. (2021). Evening side EMIC waves and related proton precipitation induced by a substorm. *Journal of Geophysical Research: Space Physics*, 126, e2020JA029091. <https://doi.org/10.1029/2020JA029091>
- Zhang, X.-J., Ma, Q., Artemyev, A. V., Li, W., Kurth, W. S., Mauk, B. H., et al. (2020). Plasma sheet boundary layer in Jupiter's magnetodisk as observed by Juno. *Journal of Geophysical Research: Space Physics*, 125(8), e2020JA027957. <https://doi.org/10.1029/2020JA027957>